ETH zürich

TECHNISCHE UNIVERSITÄT WIEN

Master's Thesis

TEM as a Tool for Bulk Metallic Glass Characterization: An Investigation into the Pt-Cu-P System

ETH Zürich, Department of Materials
Laboratory of Metal Physics and Technology

Viktor Wessely

Zürich/Vienna, April 2018

supervised by:
Prof. Dr. Jörg F. Löffler (ETH Zürich)
Dr. Robin Schäublin (ETH Zürich)
and
Prof. Dr. Herbert Danninger (TU Wien)

Abstract

The objective of this work is to contribute to establishing a deeper understanding of the relationship between the atomic arrangement in metallic glasses and its thermal stability. To study the medium-range order of amorphous materials, fluctuation electron microscopy (FEM), a hybrid imaging and diffraction technique in transmission electron microscopy (TEM) has proven to be a powerful method. This study aims to build a foundation of implementing FEM as a characterization technique at the *Laboratory of Metal Physics and Technology* (LMPT) and to perform a feasibility study on an *FEI Talos* TEM.

Different glassy alloys in the Pt-Cu-P system have been provided for this study. For future studies, a method for preparing more samples is developed and described in this work. Two more alloys with different compositions are prepared. The chemical composition of the provided samples was verified by ICP-OES measurements.

A critical part of the TEM work consists in finding and refining a preparation method that yields undamaged TEM specimens with good surface quality, so that the amorphous structure remains pristine for analysis. For that purpose, different thinning techniques, namely ion milling, FIB, ultramicrotomy and tripod polishing are tried and evaluated.

Phase transitions are studied by differential scanning calorimetry (DSC). DSC measurements are performed to obtain the total energy of fusion H_f and to determine the onset temperature of crystallization T_x and melting, T_m, and the glass transition temperature, T_g, providing information on the glass forming ability (GFA) of the alloy. Critical cooling rates for amorphization are assessed by Flash-DSC, a technique allowing for a quenching rate up to thousands of Ks^{-1}.

Scanning electron microscopy (SEM) and energy-dispersive X-ray spectroscopy (EDS) are used to characterize the microstructure of samples following DSC and quenching to investigate the various phases occurring upon crystallization. They are identified using diffraction in the TEM by matching the diffraction patterns to simulated ones from candidate structures found in literature. In addition, chemical mapping in TEM and atom probe tomography (APT) are used to evaluate the chemical homogeneity and X-ray diffraction for the overall crystalline or amorphous state.

Acknowledgments

I would like to express my gratitude towards Professor Jörg F. Löffler who kindly accepted me as a Master's student of the Laboratory for Metal Physics and Technology at the Department of Materials at ETH Zürich. He provided me with an excellent research environment. From the very first day at the LMPT I have enjoyed the open-mindedness and the ambitious scientific approach that defines his research group.

Special thanks should be given to my supervisor Robin Schäublin for providing me with unfailing support and continuous encouragement throughout the project and the process of writing this thesis. His dedication and willingness to give his time so generously have been very much appreciated. All the hours and days on the TEM as well as many joyful conversations with him have made this time very special.

I wish to acknowledge the help provided by Güven Kurtuldu. His striving for perfection is admirable and had a great impact on me. I am particularly grateful for the assistance given by Mihai Stoica. He was always open for discussion and provided me with help and guidance throughout my studies. I have particularly enjoyed working with Stephan Gerstl as his passion for science is certainly contagious.

Moreover, I would like to acknowledge the help provided by the members of the ScopeM facility. I am particularly thankful for the assistance given by Danièle Laub and her coworkers at EPFL.

It is a matter of great importance to me to extend my thanks to all the LMPT members that are not namely mentioned, yet also contributed to my work. I am grateful for all their advice and help.

Last, but not least, I would like to thank Professor Herbert Danninger, dean of the faculty of technical chemistry at Vienna University of Technology, for his confidence in my work and the cooperation throughout this project.

Contents

1 Introduction

> (...) it is a surprise to a newcomer to the field to find that there is still scope for debate about the structures of certain amorphous materials.
>
> *W. Cochran, 1973*

Knowledge of the structure of a material is critical for any understanding of its properties. It allows improvement of the material or creation of new ones with better properties. For most classes of materials a profound understanding of the relationship between atomic structure and macroscopic properties has already been developed. The structure of liquids and amorphous materials and its consequences for their properties is still only understood to a very limited degree.

Of course, this is not because researchers throughout the centuries have been ignoring amorphous materials. Amorphous solids differ from their crystalline counterparts in one major point: The absence of translational periodicity. Amorphous materials have aperiodic structures. Translational symmetry implies an enormous simplification in structural investigation. Many macroscopic properties of a crystalline solid are comprised in one nanometric unit cell that can be repeated to any extent in 3-D space.

In the 17th century people started to scientifically investigate crystals, hypothesizing that the macroscopic symmetries result from regular packing of elementary building blocks. Later, symmetry elements in crystals were discovered and in the 19th century a complete catalog of possible symmetries was established. The 14 Bravais lattices and 230 space groups were discovered long before X-ray crystallography was available. One of the first studies on the stucture of liquids in the 1960s was conducted in by J. D. Bernall, stimulating the study of amorphous solids with random packing of spheres [1]. Ever since, through dramatically increasing computation power (which allows for complex modelling) and new characterization methods, new possibilities for the advancement in the field have emerged.

1.1 A brief introduction to bulk metallic glasses

Bulk metallic glasses (BMGs) form a relatively new class of materials. They are solid, amorphous metals (usually alloys) that have a non-crystalline atomic structure. As a glass, BMGs show a glass transition that transforms a supercooled liquid state into a

glassy state when cooled and vice versa upon heating. By convention, a BMG is an alloy with a critical casting thickness of 1 mm and above[2].

The structure of metallic glasses is closely related to that of metallic melts. The non-crystalline structure can be retained if the liquid is quenched at a sufficiently high rate. The temperature has to get below the glass transition temperature before nucleation and growth of crystals. [3] The formation of the amorphous structure of many glassy alloys follows the "confusion principle". These alloys often contain three or more different elements so that upon cooling at fast rates the constituents block each other from forming the equilibrium (crystalline) state and the disordered state is kinetically preserved. Unlike silicate- or other oxide glasses that are based on tetrahedral structural subunits, metallic glasses are built from spherical components. This major structural difference required much greater cooling rates to retain the amorphous structure [4].

It wasn't until 1960 that the first metallic glass, a eutectic $Au_{75}Si_{25}$ alloy, was discovered by P. Duwez and others at Caltech [5]. The required cooling rates were on the order of $10^{-6}\,Ks^{-1}$ through a process commonly referred to as *Rapid Solidification Processing*. This includes methods like melt spinning or splat cooling and comes with great limitations in sample geometry. As heat must be extracted from the melt, the thermal conductivity of the material limits the cooling rate throughout the bulk of the material. Therefore thicknesses of over 50 µm could hardly be achieved.

It took almost three decades to overcome those limitations. In the late 1980s D. Turnbull (Harvard University), A. Inoue (Tohoku University) and W. Johnson (Caltech) developed multicomponent metallic alloys that had critical cooling rates in the range of $1 - 100\,Ks^{-1}$, which allowed samples to be prepared by either pressure or suction molding. This allowed for much more complex and larger geometries, paving the way to industrial applications. Figure 1.1 shows the development of the highest achievable critical casting thickness of any alloy available at the time. Within four decades the critical casting thickness has increased by three orders of magnitude [6].

The glass forming ability (GFA) of an alloy is closely related to the stability of its supercooled liquid. For that, A. Inoue formulated three well known empirical rules for features of a system with good GFA [7]: (1) a multicomponent system with three or more elements, (2) a significant atomic size mismatch of 12 % or more and (3) a negative heat of mixing (endothermic).

The glass forming ability of an alloy melt is governed by thermodynamic and kinetic effects. When the temperature of the melt is decreased below the liquidus temperature T_l the crystalline state is thermodynamically favorable. The Gibbs energy ΔG is the force that drives crystallization. It increases as the liquid further cools and increasingly deviates from equilibrium [3]. On the other side, nucleation kinetics becomes very slow at low temperatures and resistance to relaxation increases with the (dramatically) increasing viscosity. The competition of these opposite effects gives rise to the typical TTT

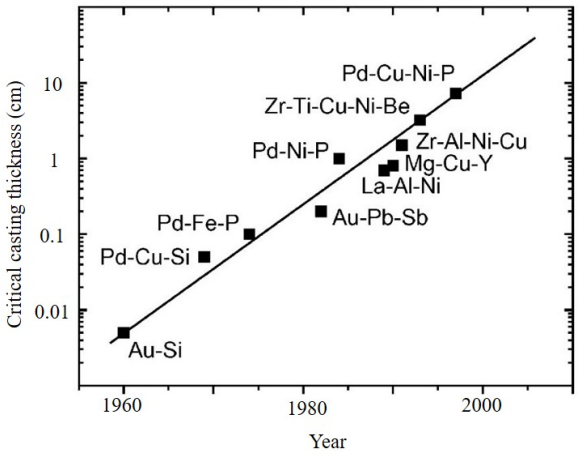

Figure 1.1: Critical casting thickness as a function of the year the alloy was discovered. From: Löffler, J. F. (2003): Bulk metallic glasses [6].

(time-temperature-transformation) diagram displayed in figure 1.2. A less steep slope of $\dot{\mathrm{T}}$ indicates an increased GFA. Therefore a high reduced glass transition temperature $T_{rg} = T_g/T_l$) aids glass formation. A narrow supercooled liquid region $\Delta T_x = T_x - T_g$, where T_x and T_g represent the crystallization and glass-transition temperatures, respectively is beneficial as well.

Metallic glasses are not at thermodynamic equilibrium. As the cooling rate determines which structure of the supercooled liquid is preserved, both the structure and the properties of a BMG are highly sensitive to its formation history [3]; annealing can lead to major structural relaxation thereby considerably altering the properties of the material. This has to be considered when performing structural investigations into BMGs.

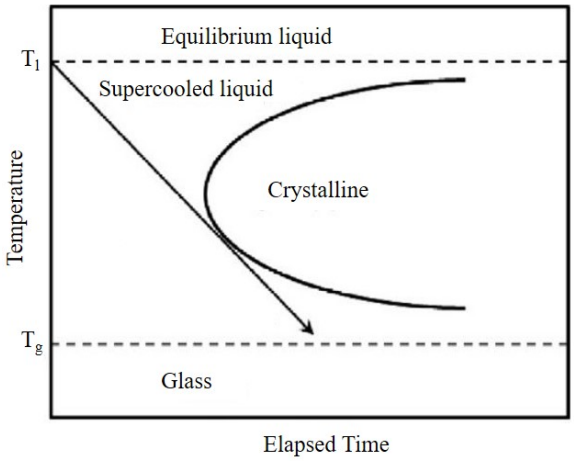

Figure 1.2: An exemplary TTT-diagram showing the process of glass formation from a stable liquid. The slope of the line, starting at t=0 indicates the critical cooling rate for glass formation($\dot{T}$). Adapted from Cheng Y. Q. et al.(2010): Atomic-level structure and structure-property relationship in metallic glasses [3].

1.2 Properties of bulk metallic glasses

Bulk metallic glasses show a variety of extraordinary properties that are continuously driving interest in research in these materials. Their mechanical, chemical, magnetic and thermophysical properties make them interesting materials for use as both structural and functional materials.

BMGs are extremely strong and elastic as they can handle large stresses without undergoing persistent (plastic) deformation. Figure 1.3 illustrates the exceptional mechanical properties. Their yield strength (the limit to which a material can be strained without plastic deformation) in combination with a high fracture toughness (the ability to resist the growth of cracks) is unreached among engineering materials, even steel. The absence of grain boundaries gives rise to superb resistance to corrosion and wear.

There is, however, a significant drawback that comes with the amorphous structure: when a metallic glass fails, it usually fails catastrophically with little or no ductility. Crystalline materials exhibit strain hardening and can distribute shear stress throughout the bulk via dislocations. Metallic glasses do not have dislocations and tend to localize shear in narrow shear bands. This causes local heating and weakening of the material, leading to even higher shear rates (strain softening) [2].

When a BMG is heated to temperatures just above T_g it relaxes into a liquid. This supercooled liquid can be processed much like a thermoplast, enabling unique opportunities in processing. As the alloys contain atoms of significantly different sizes, they,

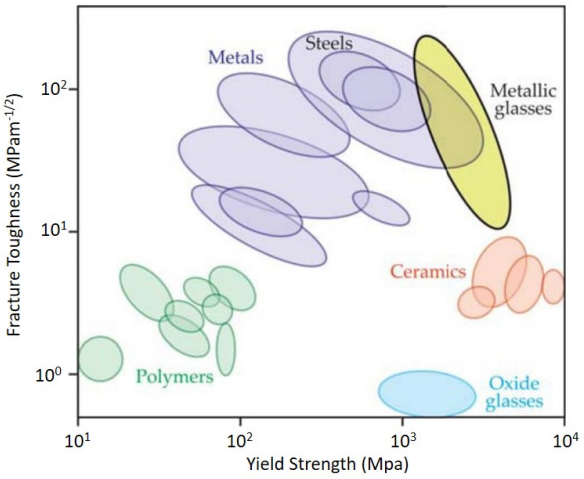

Figure 1.3: Metallic glasses are very strong materials, making them interesting for engineering applications. The diagram shows the yield strength and fracture toughness of BMGs compared to other groups of materials. Adapted from: Schroers, J. (2013): Bulk Metallic Glasses [2].

and especially their melts, show high packing densities and low free volume. Compared to common metal melts this means a greatly increased viscosity which hinders mobility and formation of an ordered lattice upon cooling. This brings another great advantage for processing, e.g. in injection molding: BMGs do not show significant shrinking upon solidification. This allows extremely small tolerances in molding and no post-molding processing (CNC) is necessary to achieve desired geometries [8].

It's not only the mechanical properties of metallic glasses that are intriguing. Like their mechanical properties, the magnetic properties are owed to their structure. As metallic glasses do not possess any magnetocrystalline anisotropy, the magnetization can be easily changed by an external field, making them a soft magnet. The energy dissipated in magnetizing and demagnetizing the material is proportional to the area covered by the hysteresis loop. Therefore, especially in high frequency transformers, the use of metallic glasses can lead to major energy savings.

Table 1.1 provides an overview on selected mechanical properties of Vitreloy 1 [4] and compares them to X5CrNi18-10 (304, V2A) steel [9] [10]. Vitreloy 1 $Zr_{41.2}Ti_{13.8}Cu_{12.5}Ni_{10}Be_{22.5}$ was developed at Caltech in the 1990s and, as one of the first amorphous alloys, commercialized by *Liquidmetal Technologies* [8].

[1] the elastic limit of a BMG is generally specified as the elastic strain limit (%)

Table 1.1: Selected mechanical properties of Vit 1 (metallic glass) and X5CrNi18-10 (steel)

Property	Vit 1	X5CrNi18-10
Elastic limit, ε_{el}	2 % [1]	-
Tensile strength, σ_y	1.9 GPa	585 MPa (UTS)
Young's modulus, E	101 GPa	180 GPa
Shear modulus, G	37.4 GPa	77 GPa
Bulk modulus, B	114.1 GPa	140
Poisson ratio, v	0.35	0.29
Vickers hardness	100 HV	129 HV
Fracture toughness, K_{Ic}	20-60 MPa $m^{1/2}$	(300) MPa $m^{1/2}$
Thermal expansion coefficient	$10.1 \cdot 10^{-6} K^{-1}$	$16 \cdot 10^{-6} K^{-1}$
Density	6.11 g cm^{-3}	7.9 g cm^{-3}

1.3 Applications

A limitation for the wider application of metallic glasses is their high cost. At about $ 100 per kilo some of the cheapest BMGs on the market are still a factor of 100 more expensive than steel [2]. This limits BMGs to applications for which not material costs but processing costs are economically relevant. These specialized applications include medical implants, electronic casings, exclusive sporting equipment, micro-electromechanical systems (MEMS), as well as watch cases and jewelery.

Due to their high elastic limit, their tensile strength and fracture toughness, BMGs are highly suited for applications that require the storage of large amounts of elastic energy. The maximum elastic energy density $E\varepsilon_{el}^2/2$ is generally 4-10 times greater than that of their crystalline counterparts [4]. This makes them very interesting for applications like sporting equipment (golf clubs, tennis rackets) and ultra-high performance springs. Similar alloys are also used to produce diaphragms for pressure sensors (for e.g. automotive) that are smaller, more sensitive and can withstand higher pressures than steel diaphragms [11].

A major application of metallic glasses is owed to their special magnetic properties. As soft magnetic materials they possess a narrow hysteresis loop and are therefore suitable to increase energy efficiency in high-frequency transformers.

1.4 Fundamental concepts of amorphous solids

Amorphous solids are best introduced by what they are not rather than by what they are: their structure is "not crystalline on any significant scale" [12], meaning they lack the long range order that is characteristic of a crystal. They do not have any translational

symmetry. They do, however, possess a significant short-range and mid-range order.

1.4.1 Crystalline solids

The fundamental concept for order in a crystalline solid is the repetition of identical groups of atoms. This group is called the *basis*, whereas the set of points in three dimensional space to which the basis is attached is known as the *lattice*. If any one point is taken as the origin for position vectors, R, all the other points are generated by a set of discrete translation operations described by:

$$R = n_1 a_1 + n_2 a_2 + n_3 a_3 \tag{1.1}$$

where n_i are integers and a_i are the primitive translation vectors. This equation represents the ordering principle for the position of all lattice points. The primitive translation vectors are often used to define the *crystal axes*, which form three adjacent edges of the primitive parallelepiped that constitutes the primitive *unit cell*. Symmetry operations yield 14 different lattice types in three dimensions, the *Bravais lattices*. The defining property of a crystal is its inherent symmetry; all crystals have translational symmetry in three directions and may have other symmetry elements as well. [12]

Crystalline solids are formed by discontinuous solidification. The solid grows in the liquid and (usually) exclusively at liquid-solid interfaces following the formation of crystallization centers, a process referred to as 'nucleation'. The rate of crystal nucleation and the speed at which the the crystal-liquid interface advances (growth) determines the crystallization rate. Both these parameters are strongly dependent on the reduced temperature T_r and the undercooling ΔT_r.

$$T_r = \frac{T}{T_m} \tag{1.2}$$

$$\Delta T_r = \frac{T_m - T}{T_m} \tag{1.3}$$

1.5 Structure of amorphous solids

Very much unlike crystals, the structure of an amorphous material does not have a uniquely defined form. The exact constituent atomic positions are not fixed, meaning that every glass is actually unique. Solving an exact structure in terms of a complete set of atomic coordinates is therefore neither desirable nor even possible. The goal when effectively studying an amorphous solid must therefor be: *Characterizing a given structure by identifying the key structural features relevant for its properties* [3]. Structural information is therefore required in the form of distribution functions, orientation relationships, bond-angle distributions, local symmetry, chemical short range order and

coordination numbers. Experimental techniques for extracting this information include diffraction (X-ray, electron, neutron), XAFS, TEM (Fluctuation Electron Microscopy, HRTEM, NBED), NMR and others.

Short range order (SRO) in the form of local arrangement of atoms can be specified through the mean bond length, the bond angle distribution and the number of nearest neighbors (the coordination number). The smallest ordered element could be, e.g. a tetrahedral or icosahedral unit. This 'local structure' is usually the immediate environment of a given atomic species to the second neighbor. A limit of 1.5 to 2 nm at which deviation from randomness occurs has been suggested. Beyond that, the structure is expected to be geometrically disordered hence there is no long-range order [13]. The ordering from the second coordination shell upwards is termed the medium-range order (MRO). It has been suggested that the MRO arises due to packing and interconnection of SRO-clusters (forming e.g. icosahedral structures) [14].

A further structural characteristic is presented by compositional ordering. In a binary A-B glass, local compositional ordering distinguishes between models where either A-B or A-A and B-B clusters are preferably formed, the alternative being a random distribution. [13]

All these structural features, giving rise to the material's properties, are determined by the relative positions of the atoms to each other. Only when the atoms are close enough to each other, they can interact. The relative inter-atomic distances r_{ij}, where i and j stand for the individual atoms, can be described by the pair density function $\rho(r)$, depicted in equation 1.4. It is here defined in terms of g(r), which is usually called either the *radial distribution function*, *the atomic pair correlation function* or the *pair distribution function (PDF)* [15].

$$\rho(r) = \rho_0 g(r) = \frac{1}{4\pi N r^2} \sum_i \sum_j \delta(r - r_{ij}) \tag{1.4}$$

In an N-atomic system, the PDF $g(r)$ provides a measure of the probability of finding a particle at a distance of r away from a given reference particle, relative to that of an ideal gas. The δ is the Dirac delta function. It is normalized so that as $r \to \infty$, $g(r) \to 1$ and $r \to 0$, $g(r) \to 0$. At distances shorter than the minimum bonding length of two atoms, the probability of finding two atoms becomes 0. The pair density function $\rho(r)$ oscillates about the average number density of the material and as $r \to \infty$, $\rho(r) \to \rho(0)$ and $r \to 0$, $\rho(r) \to 0$. For reasons of simplification, only the monoatomic PDF is discussed here. The reader has to keep in mind that for an accurate structural description of a multicomponent system, all partial PDFs must be considered.

In a material without long-range order $\rho(r)$ asymptotes to $\rho(0)$ at high values of r. At low r, the oscillations around $\rho(0)$ contain valuable structural information. Maxima are positive and minima are negative deviations from the average number density. Both

$\rho(r)$ and $g(r)$ are called *pair correlation functions* as they provide information on correlations of pairs of atoms (in the form of deviations from average behavior). Figure 1.4 shows an example of an atomic pair density function of an amorphous $Pd_{40}Ni_{40}P_{20}$ alloy.

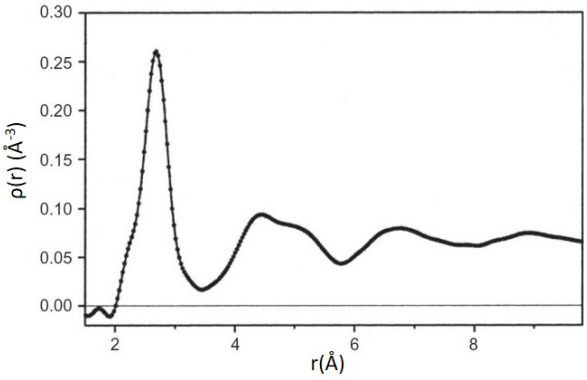

Figure 1.4: An exemplary atomic pair density function from a $Pd_{40}Ni_{40}P_{20}$ amorphous alloy. The data approaches 0 at low r and assymptotes to $\rho(o) = 0.07$ $A^{-}1$ at high r. The oscillations show a greater probability of finding two atoms at a separation distance of 2.8 Åand 4.2 Å. From Egami, T. et al. (2012): Underneath the Bragg Peaks: Structural Analysis of Complex Materials [15].

1.5.1 Structural models

Following the concept of random packing of spheres [16], different mathematical models have been developed that allow a prediction of the distribution of arrangements and coordination numbers for random clusters.

One of them is the *blocking model*, where a cluster (of equal sized spheres) is formed by the sequential addition of k spheres to the surface of the inner sphere until no more spheres can be added (the addition of further spheres is *blocked*). Following the equations for angular separation (spheres must not overlap) the probability that another sphere can be added is always equal to 1 for $1 \leq k \leq 5$. For $k \geq 6$ the probability will depend on the position of previously added spheres. Although it seems there is no analytical solution to this problem, computations on a large set of cluster samples have shown that random clusters with a coordination number of 8 and 9 occur with a probability of 85 % [1]. These computations yield a discrete function which is called the *coordination number distribution function*.

1.5.2 What is a glass?

Glasses are non-crystalline solids which are formed by continuous solidification of a cooled liquid. That means they do not undergo crystallization upon cooling from the

melt. Unlike crystals which grow at the solid-liquid interface glasses form homogeneously by the rearrangement of the atoms/molecules throughout the entire liquid [17].

Although the crystalline state is energetically preferred, there is an activation barrier and the glassy state is kinetically stabilized. A glass possesses the (random) structure of the liquid from which it was formed by cooling. In analogy to 'crystallization' the process of glass formation is often referred to as 'vitrification'. The fact that glasses are formed by cooling from a liquid, together with their presence of a glass transition, sets it apart from the general, purely structural definition of amorphous solids. These, in fact, can be formed by variety of processes, including vapor deposition.

The reversible transition between an amorphous solid and a liquid (and vice versa) is called a 'glass transition'. It has been suggested that the glass transition is a result of the material's rate of relaxation becoming a lot slower than the cooling rate. Thermodynamically a glass should always be relaxing towards either a supercooled liquid- or crystalline state [2]. When the temperature of a "normal" liquid is lowered, its volume decreases (linearly) until its melting/freezing point T_m is reached. At the phase transition (which can occur below the actual freezing point due to undercooling) there is a precipitous drop in volume as the density of the crystal is higher than that of the liquid. With further cooling, the specific volume decreases depending on the thermal expansion coefficient of the material. As shown in figure 1.5 a glass-forming liquid behaves differently. Through either a high cooling rate and/or the absence of heterogeneous nucleation sites, it is possible to achieve significant undercooling. At some point, the viscosity becomes so large that mobility and rearrangement is rendered impossible and the liquid structure is kinetically preserved ("frozen-in"). This point, the glass transition temperature T_g, is (rather arbitrarily) defined as the point where the viscosity reaches 10^{12} Pa s [11]. However, the material does not experience a sudden increase in density upon solidification.

It is critical to emphasize that the glass transition is not a transition between two thermodynamic equilibrium states. It is rather a strictly kinetic effect that is influenced by various parameters, most prominently by the cooling rate. Generally a glass is greatly affected by its preparation conditions, such as the cooling rate. As illustrated in figure 1.5 using slower cooling rates (yet still equal or above the critical cooling rate) a denser material is obtained due to the increased time for structural relaxation. Also, by reducing the cooling rate, T_g is shifted to lower temperatures. Generally though the temperature dependence of T_g is not very strong - changing the cooling rate by a magnitude will shift T_g by about 3 - 5 °C .

In his well-known paper of 1969 D. Turnbull [17] identifies the key parameters for glass formation. As solids are generally more stable in a crystalline than in an amorphous state crystallization must be bypassed. The key question remains: *Which substances can exist in glassy form and under which conditions can the crystallization of these substances be bypassed?* Primarily, the material must be brought to its glass transition temperature

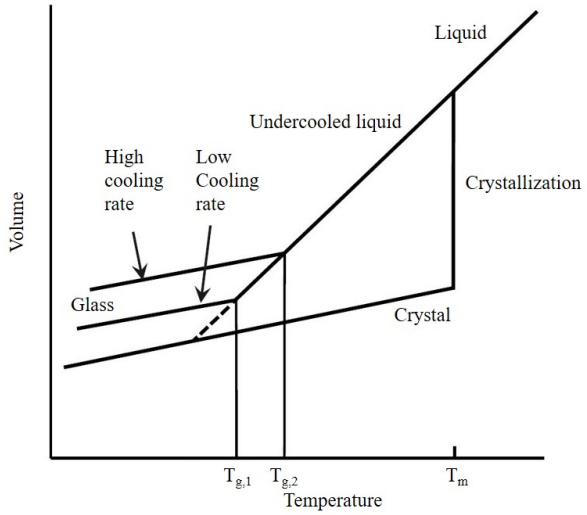

Figure 1.5: Temperature - volume diagram comparing the processes of crystallization and glass formation. T_g is located at the intersection of the cooling curve of the undercooled liquid and the glassy state, whereas lower cooling rates yield higher densities. A slow cooling rate produces a glass transition at $T_{g,1}$, a high cooling rate leads to a glass transition at $T_{g,2}$. It can be seen that the thermal expansion coefficient (the slope) of the glassy state is roughly equal to the crystalline state. From Inoue, A. et al. (2011): Bulk Metallic Glasses [11].

without crystallization. Whether or not this is possible depends on the cooling rate, the liquid volume, the seed density ρ_s, the crystal-liquid interfacial tension and the reduced glass transition temperature T_{rg} (T_g/T_l). A high value for T_{rg} will lead to enhanced glass forming ability. Intensive research has led to findings of a large number of glass forming systems; it is, however, still not known if a glassy state can be reached for every substance.

1.5.3 Challenges presented by disordered matter

Amorphous materials inherently lack a unit cell that contains all the information as for a crystal. For an exact description of the material all the coordinates of each atom are needed. Since this is not possible for systems of significant size, statistical descriptions are used, but often difficult to obtain. Diffraction experiments provide information on inter-atomic distances, but not on their spatial arrangements. [18]

Many disordered systems, like metallic glasses, are not at thermodynamic equilibrium. This means they are not uniquely defined by their composition, temperature and pressure. Factors such as thermal history and method of preparation have a great impact on material's properties. Simplifying principles that are available for highly ordered systems such as perfect order of crystalline materials, or highly disordered systems, such as

perfect randomness in gases, are not available to the same degree for disordered matter.

1.6 The Pt-Cu-P system

1.6.1 Pt-Cu-P - an excellent glass former

Over the last decades, a great number of glass forming alloys have been discovered and characterized. A group of alloys with a high glass forming ability are based on Platinum. They generally exhibit a low liquidus- and glass transition temperature. A low T_l value is important for the glass forming ability of an alloy as at an increased T_l the high mobility of the atoms in the melt makes undercooling of the melt extremely difficult.

BMGs in the system $Pt_{100-x}Cu_xP_{20}$ can be generally characterized as metal-metalloid type. This nomenclature has prevailed in the BMG community and indicates the nominal composition in mole-%. According to the classification introduced by Inoue and coworkers [19], Pt-Cu-P BMGs are described as LTM-NM-type (late transition metal - non metal). They have a high reduced glass transition temperature and large supercooled liquid region, promising a good glass forming ability. As a multicomponent BMG they also derive their high glass forming ability from destabilization of competing crystals.

For BMGs in the system $Pt_{100-x}Cu_xP_{20}$ the glass transition temperature has been found to increase with rising Cu content, with a maximum of 249 °C at 20 % Cu. The crystallization temperature T_x rises with increasing Cu-content until reaching level of saturation at 25 % Cu and 325 °C. The supercooled liquid region increases from 25 °C (0 % Cu) to 83 °C (35 % Cu). The lowest liquidus temperature T_l is measured at 581 °C resulting in a maximum T_{rg} value of 0.61 [20]. The highest GFA is therefore expected to occur at Cu contents between 20 and 25 %.

Bulk metallic glass formation has been found most effective at or near their eutectic points and less favorable for off-eutectic alloys [21]. The eutectic composition in the system described lies at a nominal composition of $Pt_{57}Cu_{23}P_{20}$ [22]. Figure 1.6 provides information on the measured and estimated critical casting thickness of PtCuP-alloys.

1.6.2 Structure of LTM-NM metallic glasses

The structure of different LTM-NM BMGs has been studied; structural models were based on the concept of dense random packing of hard spheres (DRPHS model). Further refinement suggested strong chemical ordering which could not be explained by the DRPHS-model alone [23]. In these models, SRO (to the first coordination shell) is well defined and chemical ordering is almost identical to the corresponding crystals. The difference lies in the MRO, which is defined by the packing of the stereochemical units. This model describes the stereochemical units in e.g. Ni-P based glasses as tri-

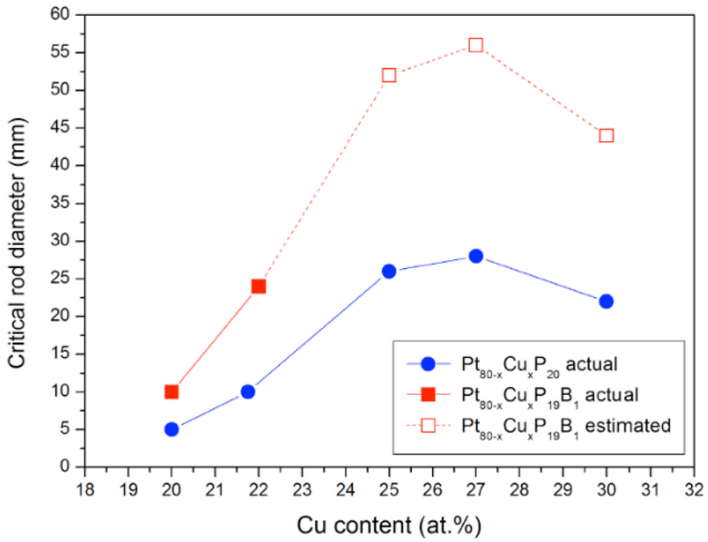

Figure 1.6: Critical casting diameter of PtCuP alloys. Addition of small amounts of boron is expected to significantly increase GFA. [22]

capped trigonal prisms (TTP) with nine Ni-atoms in the shell and one central P-atom. It has been suggested that these TTP-units are connected in a chain by sharing their edges.

Early models derived from DRPHP are based on the assumption of a single, crystal-like stereochemical unit with a fixed coordination number and uniform bond lengths. More recent models identify a number of structural characteristics in LTM-NM metallic glasses. Strong chemical ordering with solute-solute avoidance has been confirmed, but it has been found that the SRO around the solute (NM) is not necessarily the same as in the corresponding crystal. It is rather strongly influenced by the effective size ratio between the solvent and the solute [24]. The concept of a single cluster type is replaced by a distribution of various cluster types. The MRO arises due to dense random packing of these clusters by face-, edge- or vertex sharing [25], forming icosahedral-like superstructures.

Based on binary LTM-NM metallic glasses, there are multiple multicomponent systems. Solving the structure of a multicomponent BMG is generally very challenging as a great number of interactions have to be considered. Investigations into the Pd-Ni-P system [25] have revealed that the LTM-atoms mix randomly, greatly decreasing chemical ordering compared to the binary system. The same study finds nanoscale fcc-like clusters embedded in an amorphous matrix of P-centered TTP-units [3]. This means, the BMG is chemically heterogeneous and shows nanoscale phase separation with supercritical nuclei. Since these features are very small, they cannot be detected easily. Conventional diffraction techniques (XRD, SAED, neutron diffraction) only provide averaged information due to their limitations in probe size which means the essential local structural

Table 1.2: Crystal data of possible candidate structures of the recrystallized Pt-Cu-P alloy, obtained from the *Inorganic Crystal Structure Database* provided by *FIZ Karlsruhe*.

Structure Formula	Space Group (HMS)	Structure Type
Pt	F m -3 m	fcc-Cu
Cu	F m -3 m	fcc-Cu
PtP_2	P a -3	Pyrite-FeS_2
Pt_5P_2	C 1 2/c 1	
Pt_7Cu	F m -3 m	Ga_7Ge
Cu_3Pt	P m -3 m	$AuCu_3$
CuPt	F m -3 m	fcc-Cu
CuPt	R -3 m H	HgIn
Cu_3P	P 63 c m	LaF_3
Cu_2P_7	C 1 2/m 1	
CuP_2	P 1 21/c 1	CuP_2
Cu_2P_{20}	P -1	
Cu_3P	P -3 m 1	Cu_3P
Cu_3P	P -3 c 1	Cu_3As

information is lost. By precisely controlling the probing beam size, fluctuation electron microscopy (see section 2.4.2) may overcome these limitations.

1.6.3 Binary phases

The ternary Pt-Cu-P alloys have been reported to crystallize through a single-stage exothermic reaction forming precipitates of Pt_5P_2, Cu_3P and unidentified phases [20]. Crystallization from the stable liquid most likely yield different phases. The attempt and procedure to identify those phases will be described in this work.

The phase diagrams for the binary systems are shown in figure 1.7, 1.8 and 1.9 [2]. Unfortunately there are no ternary phase diagrams available in literature. To determine the stable binary phases that occur upon crystallization, crystallography databases (ICSD) have been searched for crystal data of the binary phases. From these, .cif files (crystallographic information file) could be created which contain the lattice parameters, atomic positions and the crystal symmetry. This information allows for the simulation of the electron diffraction patterns using software such as *Crystal Maker* or *CrysTBox*, both described in section 2.6. Table 1.2 lists all the crystal structures that have been used to simulate SADPs. Phases in the recrystallized samples have been identified by matching the simulated SADPs to the experimental ones.

[2]Phase diagrams have been obtained from http://www.himikatus.ru/art/phase-diagr1/diagrams.php, accessed September 2017.

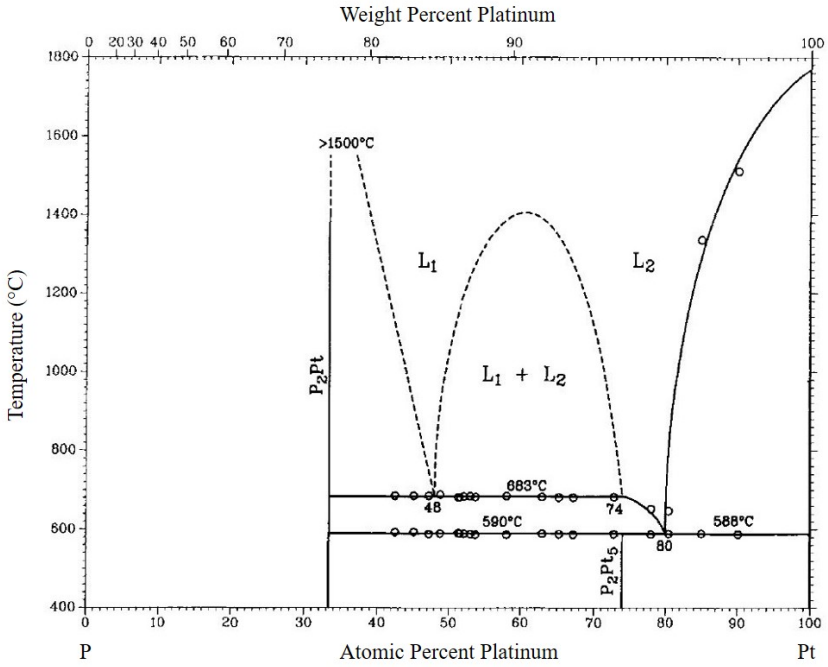

Figure 1.7: Equilibrium phases in the Pt-P binary system. It shows a miscibility gap for the liquids and two stable binary phases: the cubic PtP_2 and the monoclinic PtP_2. Due to the high vapor pressure of phosphorus at the given temperatures, the P-end of the phase diagram is not shown.

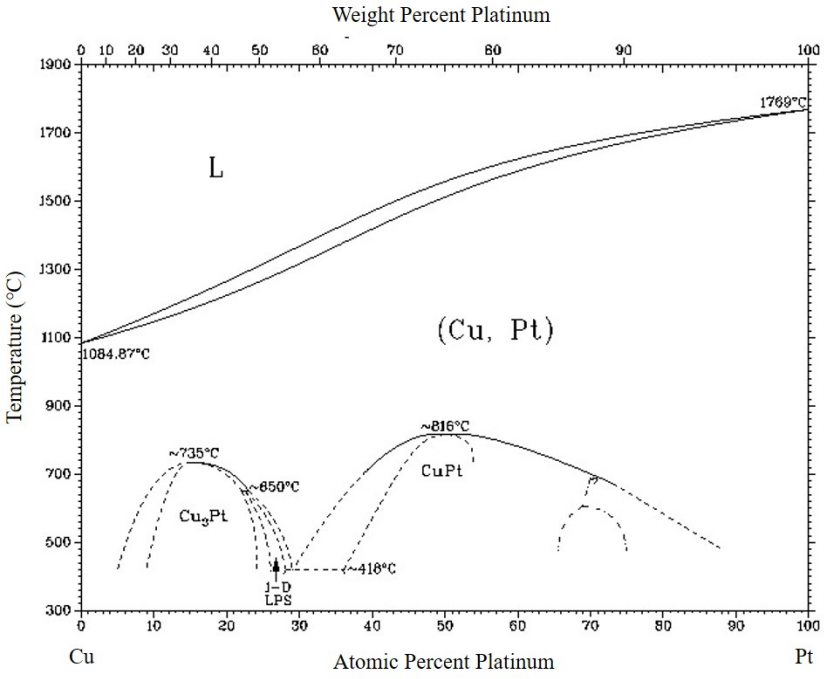

Figure 1.8: Equilibrium phases in the Cu-Pt binary system. Cu and Pt form a continuous fcc solid solution without a miscibility gap. Both phases CuPt (fcc) and Cu_3Pt ($AuCu_3$-structure, $L1_2$) occur over a range of compositions. A long-period superlattice (LPS) has been proposed in the in region of 24 to 26 at.% Pt alloys.

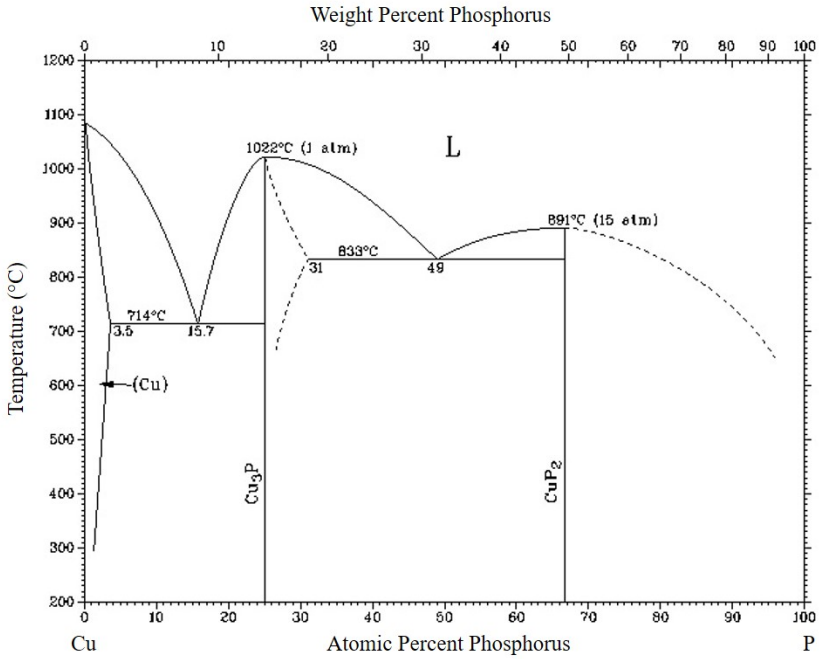

Figure 1.9: Equilibrium phases in the Cu-P binary system. Two eutectics, one between Cu-Cu_3P and the other between Cu_3P-CuP_2, can be identified. The solubility of P in (Cu) is approximately 3.5 % at the first eutectic temperature. The liquidus line between CuP_2 and P cannot be determined due to the high vapor pressure of P. Because the stable conditions of various allotropic forms of phosphorus are not very well defined, the P-rich end of the phase diagram is not presented.

2 Experimental

This section gives an overview on the experimental part, guiding the reader through sample preparation and provides information on the applied characterization techniques and equipment used throughout this study.

2.1 Samples

Three different compositions in the system $Pt_{100-x}Cu_xP_{20}$ have been provided by the research group of Prof. W. L. Johnson from the California Institute of Technology. All samples have been prepared in a quartz tube in a one-stage casting process. To avoid sublimation of phosphorus, the quartz tube is thinned at the bottom where P is placed with Pt and Cu on top. Using an induction coil, it is possible to melt the metals (with P out of the coil) thereby forming a seal above the phosphorus which subsequently dissolves in the melt. The melt contained in the quartz tube is subsequently quenched in water. Figure 2.1(f) shows both a 2 mm and a 3 mm rod from this process. The cooling rate achieved for this process is typically around 100 Ks^{-1} [26], which means that this technique can only be used to produce rods in those systems that have a high glass forming ability (low critical cooling rates for the formation of the fully glassy phase). For good glass formers, water-quenching in glass tubes allows for relatively large samples. A BMG in the Pd-Cu-Ni-P-system with a mass of more than 3 kg and a diameter of 80 mm, the largest glassy alloy ever produced, was prepared by this method [27].

Two samples of different compositions have been cast using this method: The ternary eutectic with a nominal composition $Pt_{57}Cu_{23}P_{20}$ and an off-eutectic $Pt_{55}Cu_{25}P_{20}$. From the ternary eutectic sample ($Pt_{57}Cu_{23}P_{20}$), a non-annealed and a stress annealed sample have been provided. In stress annealing, the sample is held at the glass transition temperature (235 °C) for a certain amount of time (10 - 15 h) in a tube furnace to relieve the internal stresses of the sample that arise from quenching.

2.1.1 Alloy preparation

In order to evaluate the feasibility of producing our own PtCuP alloys at LMPT, some samples were prepared on a trial basis. Following the estimates of compositions with very high GFA (see figure 1.6), alloys of nominal compositions $Cu_{53}Cu_{27}P_{20}$ and $Cu_{53}P_{27}P_{19}B$ were prepared from PtP, CuP pre-alloys and elemental metals in an arc melter. The arc melter operated under a titanium gettered, ultrahigh purity argon atmosphere (see figure 2.1). Table 2.1 provides information on the precursors that were used for further

Table 2.1: Supplier and grade of precursors for alloy preparation

	Atomic mass[1](g/mol)	supplier	purity	comments
Platinum	195.084	UBS		
Copper	63.546	Alfa Aesar	99.999	wire 1 mm, O_2 free
CuP	30.974	Alfa Aesar	-	85:15 wt., shots
Boron	10.81	Materion	99.5	3 - 8 mm pieces

alloy preparation. The alloys were cooled, flipped and remelted twice to ensure compositional homogeneity. They were subsequently cast into copper molds to form ingots 3 mm in diameter.

The PtP pre-alloy was prepared by melting Pt and P in a quartz tube. With the aim to stay in the two-phase region of Pt_5P_2 and Pt, not more than 74 % wt. Pt was used, expecting the loss of a few percent of P. The melting point of the Pt-P eutectic (at x = 0.8 Pt) lies at 590 °C. To determine a reasonable heating profile, it is critical to know the expected vapor pressures. Equation 2.1 describes the vapor pressure of P above 450 °C. [28] At 450 °C the vapor pressure is 6 bar, at 500 °C 15 bar and at 590 °C 67 bar. To minimize the risk of the quartz tube bursting due to the high pressure, after evacuation and sealing, the tube was placed in a steel tube that was then filled with argon at 5 bar to reduce the pressure difference inside and outside the tube upon heating. The tube was subsequently heated in a furnace, starting at 500 °C for 19 hours, then 560 °C for 3 hours with a final heating above the melting point at 690 °C for 4 hours. To eliminate any possible white phosphorus, the temperature was then reduced to 300 °C and held for another 3 hours before cooling.

$$\ln p = -(10.8 \pm 0.4) \cdot \frac{10^3}{T} + (16.5 \pm 0.6) \tag{2.1}$$

Starting from 20.300 g of Pt and 0.537 g of P, an alloy with a mass of 21.033 g was obtained. Assuming that all of the lost material is P, 9 mg (or 1.7 %) of phosphorus was lost during the alloying process, yielding an alloy of 79.4 %at. (96.0 %m) Pt and 20.6 %at. (4.0 %m) P.

2.1.2 Compositional analysis: ICP-OES

The procedures described in this section were carried out at the *Institute of Terrestrial Ecosystems, ETHZ* with kind permission of Björn Studer.

In order to determine the chemical composition of both the alloys provided and made,

[1]National Institute for Standards and Technology: https://www.nist.gov/pml/periodic-table-elements, October 2017

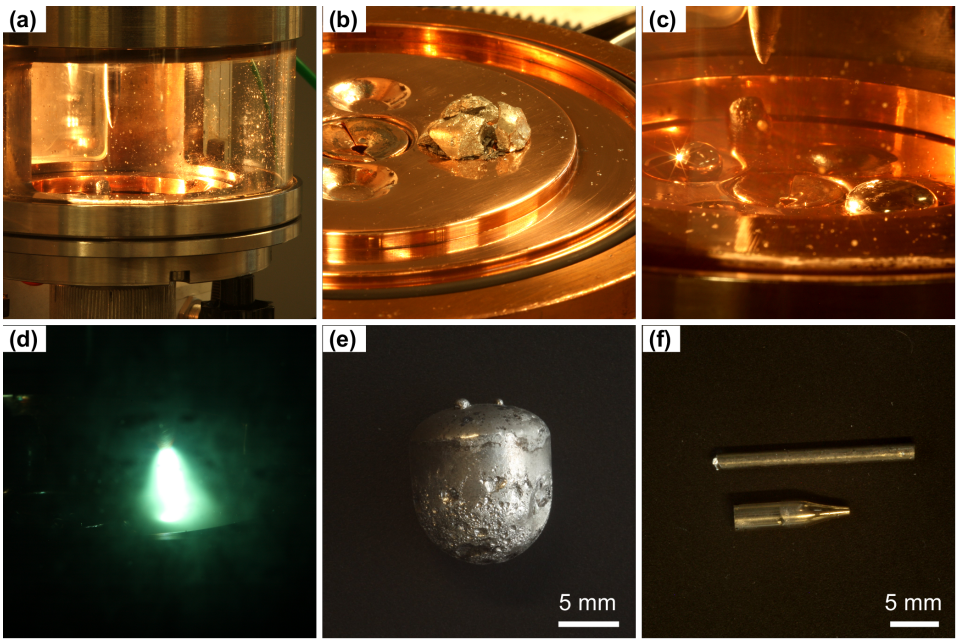

Figure 2.1: (a) shows the arc melting chamber with a water cooled Cu-base and a W-electrode. The following pictures show the alloy components before (c) and the alloy after melting (c) with the Ti-getter visible inside the chamber. (d) electric arc. (e)Pt-P pre-alloy prepared in a quartz tube. (f) $Pt_{57}Cu_{23}P_{20}$ samples prepared by water quenching in a quartz tube provided by W. L. Johnson, Caltech.

energy dispersive X-ray spectroscopy proved to be problematic for various reasons described in section 2.3. A deviation of 10 % and more in the EDS-results from the expected composition required a wet-chemical analysis of the samples for verification of the compositions.

With a Cu, P, B - multielement standard in stock, only Pt-standards had to be prepared by dissolving Platinum and diluting accordingly. Both the Platinum as well as the samples were put in Teflon tubes, adding 3 ml of acqua regia. The sample tubes were then placed in a microwave high pressure digestion system with a set peak temperature of 220 °C at 30 bar for 10 minutes. None of the amorphous samples dissolved, whereas both the Pt as well as a recrystallized BMG sample (from an earlier DSC analysis) dissolved without residue (see table 2.2).

In preparation for ICP-OES measurement, the obtained solution from the one sample that had dissolved was diluted to a total concentration of 10 mg/l. The measurement was performed on a *Agilent Technolgies 5100 ICP-OES* with a CaF_2-prisma, echelle grating and a CCD-detector possessing a wavelength resolution of 7 pm at 202.032 nm (Mo) and 13 pm at 327.396 nm (Cu).

Table 2.2: Digestion of samples

sample	dissolve YES/NO
$Pt_{55}Cu_{25}P_{20}$	NO
$Pt_{57}Cu_{23}P_{20}$	NO
$Pt_{57}Cu_{23}P_{20}$ anneal	NO
$Pt_{53}Cu_{27}P_{20}$	NO
$Pt_{53}Cu_{27}P_{19}B$	NO
$Pt_{55}Cu_{25}P_{20}$ recryst.	YES

2.1.3 XRD measurements

X-ray diffraction (XRD) is a widely applied characterization technique, especially in crystallography. It is based on observing the scattered intensity of an X-ray beam hitting a sample as a function of the momentum transfer of the scattered particle q, the scattering vector. It is defined as the difference between the wave propagation vectors of the incident and the scattered beam according to $q = k_{init.} - k_{final}$. The scattering vector itself is a function of incident and scattered angle as well as the wavelength (see equation 2.2).

$$q = \frac{4\pi \cdot \sin(\theta)}{\lambda} = k_{init.} - k_{final} \tag{2.2}$$

Historically developed from single crystal analysis, XRD measurements nowadays provide structural information on all kinds of complex materials, including glasses. X-ray measurements are usually carried out in an X-ray diffractometer where the sample is placed in the beam and rotated continuously. By convention (in crystallography) the angle between the crystalline planes and the incoming beam is referred to as the *Bragg angle* θ; the diffracted intensity is recorded as a function of the diffractometer angle 2θ. For the measurement of amorphous materials, the same setup is used, with the intensity measured as a function of 2θ. Figure 2.2 shows an exemplary diffractogram of an amorphous material.

A diffraction pattern for an amorphous material presents diffuse rings, with a wide first diffraction maximum, and several others that diminish quickly with increasing distance to the transmitted beam. The measured scattering intensity can be related to the total structure factor using equation 2.3, where $I_c(q)$ is the coherent scattering intensity and $\langle f \rangle = \sum c_\alpha f_\alpha$ the average atomic scattering factor [15]

$$S(q) = \frac{I_c(q) - \langle f^2 \rangle + \langle f \rangle^2}{\langle f \rangle^2} \tag{2.3}$$

The (reciprocal space) total structure factor $I_c(q)$ can be directly converted into the (real space) reduced pair density function G(r) via a Fourier transformation. [3] Although insufficient for the reconstruction of the three dimensional structure for multi-

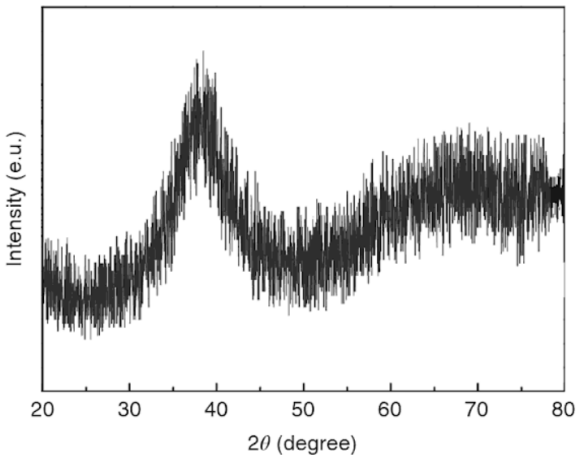

Figure 2.2: Exemplary diffractometer recording of an amorphous material showing a wide first diffraction maximum and (unlike its crystalline counterpart) no discrete peaks. From: Stachursky(2015): Fundamentals of Amorphous Solids [1]

component materials, (as it requires partial pair distribution functions), G(r) provides a good starting point for calculation of interatomic distances and coordination number [29].

These measurements are usually carried out at a synchrotron; the shorter wavelength and extremely high flux enable observation over a much larger q-range (hence smaller spacings) at a greatly increased sensitivity which allows detection of weak signals from strong scattering above the background.

All measurements presented here have been carried out on a *PANalytical Empyrean* instrument using Ni-filtered Cu-Kα X-rays with a mean wavelength from Kα_1 and Kα_2 of λ=1.54184 Å. They cannot provide the same degree of information as synchrotron XRD data could. Measurements were performed within a q-range of 0 to 6 Å^{-1} only; unfortunately only larger values of q contain the SRO information. Therefore, calculating the total structure factor and the reduced density function is feasible as a mathematical process, but it would not yield any useful data on the SRO.

2.2 Thermophysical properties

2.2.1 Differential scanning calorimetry

Differential scanning calorimetry (DSC) is a thermo-analytical method whereby the difference in the amount of heat required to increase (or decrease) the temperature of a sample relative to that of a reference is measured as a function of temperature or time. It is widely used for determination of heat capacities, enthalpies of phase transition and phase transition temperatures.

The instrument used throughout this study was a *Mettler Toledo DSC1/700*. The software used for evaulation was Mettler Toledo's *STARe*.

DSC calibration

DSC measurements are influenced by a number of boundary conditions such as the temperature range, the scanning rate, the heat flow rate, the thermal conductivity of the sample, the sample mass and other parameters. Therefore, the quality of the data obtained from measurements depends on the operational procedures and a proper calibration. Suitable calibration substances cover a large temperature range and ideally are materials that define the fixed points of the International Temperature Scale of 1990 [30]. Table 2.3 shows the values for temperature calibration of the instrument and table 2.3 shows the values for the enthalpy calibration. Reference values have been obtained from [30]. The linear regression functions that were used for correction of the measured values are given in figures 2.3 and 2.4.

Table 2.3: DSC calibration of temperature using well defined melting points of high-purity metals.

Calibration material	T_m (literature) (°C)	T_m (measured) (°C)	ΔT_m (°C)
Sn	231.928	235.3 ± 0.1	3.4
Bi	271.4	275.0 ± 0.0	3.6
Zn	419.527	423.9 ± 0.5	4.3
Al	660.323	666.3 ± 0.1	6.0

Table 2.4: DSC calibration of melting enthalpies using well defined values of high-purity metals.

Calibration material	H_m (literature) (J/g)	H_m (measured) (J/g)	ΔH_m (J/g)
Sn	60.4	56.4 ± 0.8	4.0
Bi	53.83	50.0 ± 0.2	3.6
Zn	108	101.5 ± 1.8	6.5
Al	398.1	385.2 ± 2.3	12.9

Fast DSC

Fast differential scanning calorimetry (FDSC, often also referred to as Flash-DSC) represents a complementary method to DSC. Allowing for heating and cooling rates of up to 10^5 Ks^{-1} and above it allows investigating thermophysical phenomena that are not accessible with any other technique. It is a powerful tool for characterization of metallic

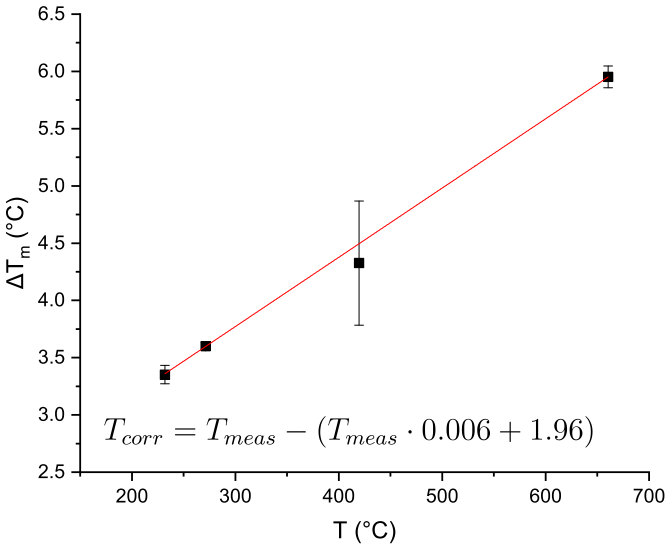

Figure 2.3: Calibration of DSC with respect to temperature. The indicated correction function was obtained though linear regression. It shows the deviation of the measured temperature from the actual value. The large error for zink is assumed to arise due to its high vapor pressure.

glasses as it allows observing in-situ glass formation and the formation of metastable phases while measuring melting enthalpies and temperatures. In many cases, these samples can be further analyzed using e.g. TEM. In this study, FDSC is used to determine the critical cooling rate of a $Pt_{57}Cu_{23}P_{20}$ metallic glass.

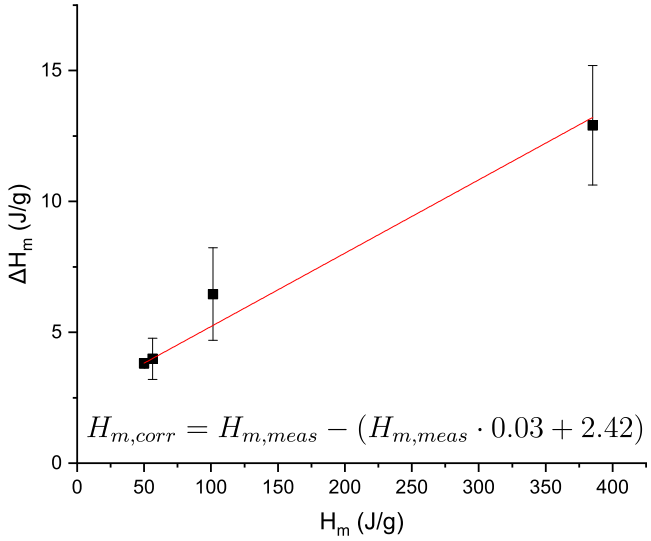

Figure 2.4: Calibration of DSC with respect to enthalpy. The indicated correction function was obtained though linear regression.It shows the deviation of the measured enthalpy from the actual value.

2.3 Scanning electron microscopy and microstructure analysis

The scanning electron microscope (SEM) is a type of electron microscope that produces an image by scanning the sample in a raster pattern with a focused electron beam. It is a widely employed technique in materials characterization as it provides a variety of information on the sample's topography and composition. When electrons enter the surface they are scattered in all directions, within a certain volume of interaction, forming an 'excitation bulb'. There are three major processes that can be observed:

Back-scattered electrons (BSE) originate from elastic scattering of primary electrons. As products of elastic collisions, they carry the same amount of energy as the primary electrons (typically a few kV). The backscatter intensity in a given area depends on the average atomic number of the present elemental species. Phases with higher average atomic numbers produce brighter areas in the picture as those atoms reflect more electrons - an effect that provides limited (qualitative), but still very useful compositional information on a sample.

Secondary electrons (SE) result from inelastic collisions of primary electrons with the atoms of the sample surface and carry little energy. Since the intensity is strongly dependent on the angle of incidence, SE can be used for surface morphology characterization.

Characteristic X-rays, which allow for energy dispersive X-ray spectroscopy (EDS), are produced by excitation of core electrons and subsequent transition of high energy electrons to the vacant lower energy state. The resulting characteristic radiation can be used for elemental characterization and quantification.

2.3.1 EDS

Energy-dispersive X-ray spectroscopy (or electron probe X-ray microanalysis) is an analytical technique used for the elemental characterization of a solid sample. It relies on X-ray excitation by a high energy electronic beam. Its characterization capabilities are based on the fundamental principle that each element has a unique electronic structure and therefore a unique set of peaks on its characteristic X-ray emission spectrum. EDS relies on the instrumentation setup of an electron microscope attached to an energy-dispersive detector.

The theory of EDS as well as scanning electron microscopy (SEM) is based on the interaction of electrons with solid matter. When an atom has been ionized by electron bombardment – for example, by ejection of a K-shell electron – the hole generated can be filled by an electron of the L-shell. There is a certain probability that the energy set free by this process will lead to the emission of a characteristic X-ray photon (Kα-radiation for the transition described). If an M-shell electron fills the vacant K-state, Kβ -radiation can be observed. A process that competes with the emission of X-rays is the emission of Auger electrons corresponding to the process of transfer of energy to another electron, which is then ejected from the atom. The fluorescence yield of X-rays increases with atomic number Z, while the portion of emitted Auger electrons behaves contrary. [31]

The physically allowed transitions are determined by the following quantum-mechanical selection rules: $\Delta n \neq 0$, $\Delta l = \pm 1$, $\Delta j = 0, \pm 1$ where n is the principal quantum number, l the angular momentum quantum number, and $j = l \pm s$ the total angular momentum. These selection rules enable the prediction of all possible transitions between electronic levels, hence the corresponding X-ray lines.

Detectors for energy-dispersive X-ray spectroscopy are capable of counting the X-ray photons that reach the detector and simultaneously measure their energy. These can either be Si(Li)-detectors (lithium-drifted Si crystals) or a high-purity Ge-crystal. These are materials that allow for the generation of electron-hole pairs by X-ray excitation. The energy necessary to create one electron-hole pair is only a few eV and as the energy of X-rays can be several keV, a single X-ray photon can create thousands of electron-hole pairs. Therefore, the energy of the incoming X-rays can be measured via the number of holes and electrons. To minimize the portion of thermally activated electron-hole pairs, detectors are usually cooled by liquid nitrogen or a Peltier cooling.

2.4 Transmission electron microscopy

Transmission electron microscopy (TEM) is a microscopy technique that is based on electrons being transmitted through a thin specimen to form an image. TEM is an extremely versatile tool for the characterization of materials from the micrometer level down to the atomic scale.

The ability to switch between different operating modes is probably one of the strongest assets of a TEM. It is possible to obtain real space (imaging mode) and reciprocal space (diffraction mode) information almost simultaneously. That allows producing images of the sample and gathering information on the crystal structure and the orientation from the same region. Combined with EDS or EELS, the collection of information on the chemical identity is possible as well. This ability makes TEM an indispensable tool in many fields ranging from applications in biosciences to dislocation analysis in metallurgy.

A transmission electron microscope consists of a number of components. To get the maximum out of this complex instrument it is critical for the operator to understand how the different controls affect the optics in the column, and ultimately the picture on the screen. Therefore, a short overview on the different parts of a TEM, from the top of the column to the bottom, is given in the following. [32]

In the **electron gun**, electrons are generated and accelerated. It provides a stable beam on electrons of controllable energy. The three main types of electron sources, thermionic- , thermal field emission and cold field emission guns greatly differ in brightness and energy spread they deliver and their price. Together with the **condenser system** the electron gun forms the **illumination system**. The condenser system consists of different electromagnetic lenses and apertures that control spot size, brightness, convergence angle (parallel for CTEM, convergent for CBED and STEM). A series of coils allow for shifting the beam and correcting tilt and astigmatism. They ensure that the optical axis is centered and the beam is symmetrical.

The **specimen stage** sits right in between the illumination and the imaging system. The specimen is inserted into the column using special sample holders, of which there is a great variety. Functionalities of specimen holders include multiple axis tilting, heating, cooling, electrical measurements and more.

The imaging system consists of a series of lenses and apertures. The first one, the **objective lens** (OL) is a multicomponent lens that sits above and below the specimen. It forms the images and diffraction patterns that are magnified by the lenses further down the column. Located in the back focal plane of the OL is the *objective aperture* (OA). By blocking scattered electrons, it allows to use the direct beam made of unscattered electrons to form a bright field image. Positioned in the image plane of the OL (and the object plane of the intermediate lens) is the **selected area aperture** (SA). It is used to define the area of interest from which a diffraction patters is desired. It is the

most common TEM diffraction technique and consequently called selected area electron diffraction. Changing the strength of the **intermediate lens** allows to switch between imaging and diffraction mode and the the **projector lens** magnifies the image onto a camera or a viewing screen. A schematic of the imaging system is presented in figure 2.5.

2.4.1 TEM: The operating modes

One of the main strengths of TEM comes from its ability to switch between different operating modes, allowing the user to access a great spectrum of informations. Changing between real-space information (imaging) and reciprocal-space information (diffraction) can be achieved by the push of a few buttons.

Diffraction yields electrons that are all coming off at the same angle as the sample is basically "grating" the electron wave as it comes in. Waves of electrons at particular angles will experience constructive reinforcement. Consequently, after passing through the specimen, parallel rays of electrons are focused to a point in the back focal plane of the objective lens. The intermediate lens (IL) has two settings: by changing its strength, and therefore its focal distance, it allows selecting either the back focal plane or the image plane of the OL as its object plane that is then projected further down the column, thereby switching between image and diffraction mode. These planes are highlighted in figure 2.5.

In **bright field imaging mode** (BF) the objective aperture is positioned in the back focal plane of the OL. It allows cutting out all scattered electrons, enhancing contrast. It also allows reducing aberrations as electrons that have been scattered at a high angle are experiencing stronger aberrations than others. In a BF-image only the beam of unscattered electrons contributes to the image. This means that regions that scatter strongly will have less electrons contributing to the image, hence appear darker. This mechanism is not only used to produce high-contrast images due to mass-thickness contrast, but is also suitable to identify the optimal tilting conditions in diffraction analysis due to diffraction contrast.

When switching from imaging mode to **diffraction mode**, the current in the IL is changed so that the back focal plane of the OL becomes the object for the IL. As the OA blocks all non-direct beam electrons, the OA has to be retracted. To select the region of interest from the sample, a selected area aperture is inserted. The main reason for the SA is that it is not advised to simply illuminate the area of interest, as one wants to preserve a parallel (non-convergent) beam.

Scanning transmission electron microscopy

Scanning transmission electron microscopy (STEM) is a TEM technique that is implemented in many modern systems. Unlike conventional TEM, STEM uses a highly

convergent probe produced by the condenser system that is scanned over the sample in a raster using a pair of deflector coils. As a major difference to TEM, STEM images are not magnified by lenses. Magnification is only determined by the size of the scanning area. As a consequence images are not affected by lens aberrations in the imaging system.

A routinely used detection mode involves a so called high annular dark-field detector, that is a ring-shaped detector that lies outside of the path of the directly transmitted beam. Given a proper alignment and high-quality probe-forming optics, high-angle annular dark field (HAADF) mode may produce images with atomic resolution. Furthermore HAADF images contain chemical information due to the sensitivity of the atomic scattering factor with respect to the atomic number Z (Rutherford scattering) in the form of "Z contrast". Atoms with higher Z scatter more strongly than light atoms, resulting in an increased intensity in the image. Bright areas/spots indicate regions or atoms with a high Z.[33]

HAADF STEM cannot provide direct quantitative information on the concentrations of different elements in a material. Combining STEM with spectroscopy further expands analytical capabilities of the instrument: chemical mapping using energy dispersive X-ray spectroscopy in STEM-mode is a powerful technique in analyzing identity and position of atoms (or rather: atomic columns) at high resolution [34].

When it comes to providing quantitative results STEM-EDS suffers from similar limitations as its SEM based equivalent. Varying X-ray fluorescence yields and absorption for the different characteristic lines make obtaining accurate quantitative yields difficult. Especially light elements, where X-ray yields are low and due to the limited energy resolution (about 130 eV), can only be quantified with great difficulty. The interaction of the electron beam with the material could be described as very complex, though due to the low thickness of the specimen however, effects such as self-absorption and and X-ray (secondary) fluorescence are greatly reduced compared to SEM EDS. Furthermore, the interaction volume is a lot smaller and spatial resolution therefore greatly improved.

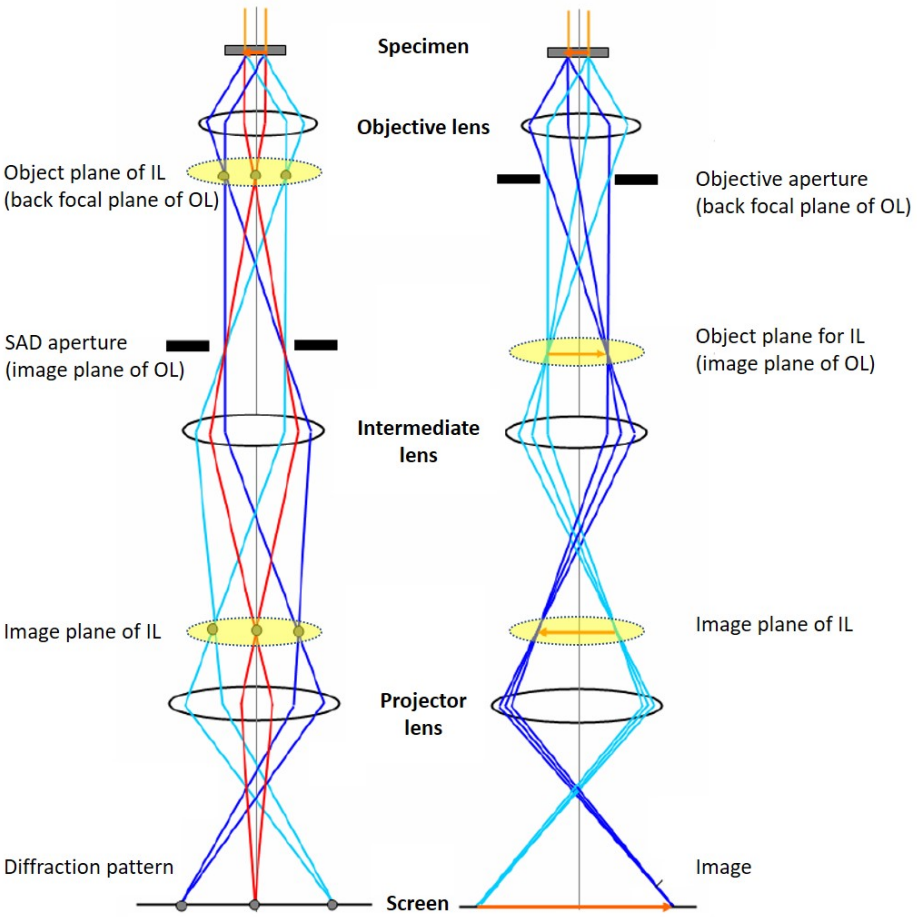

Figure 2.5: Ray diagram in diffration (left) and imaging (left) mode of a TEM. Rays scattered in the same direction are represented by one color. In imaging mode, electrons originating from the same point on the specimen are depicted in the same color. The figure has been adapted from Wepf et al. (2019): Introductory Transmission Electron Microscopy Primer for Users of EMEZ-TEMs [32].

2.4.2 Fluctuation electron microscopy

Fluctuation electron microscopy (FEM) is an electron microscopy technique for studying medium-range order in amorphous materials. The dimensions of interest are on the order of 1 nm, generally about 0.5 to 2 nm. FEM was first used to detect structural inhomogeneity in amorphous silicon, germanium and carbon, but it has as well proven to be a powerful method for characterizing metallic glasses, e.g. when it was successfully applied to characterize amorphous $Cu_{64.5}Zr_{35.5}$ [35].

It is very difficult to obtain medium-range information using standard diffraction methods. Due to the isotropic nature of disordered materials on a larger scale, they only provide averaged information due to their limitations in probe size, which means the essential local structural information is lost. The pair correlation function g, although useful to describe SRO, becomes ineffective at MRO length scales.

There are two different approaches to FEM. One is based on hollow-cone dark-field imaging (HCDF), the other one is based on diffraction in scanning TEM (STEM). Since the hollow cone tilt angle controls the coherence volume of the scattering geometry, the HCDF technique is usually referred to as **variable coherence microscopy (VC-FEM)**. In VC-FEM, the resolution R remains constant while the variance is measured as a function of the scattering vector q. The resolution matches the dimensional scale of the local fluctuations. Depending on the extent of the local coherence, the intensity of speckles changes. In STEM-FEM the probe size that controls the sample analysis volume is varied. Measuring the variance at a constant q and a variable resolution R is consequently called **variable resolution microscopy (VR-FEM)** [36].

Compared to HCDF-FEM carried out in conventional TEM mode, VR-FEM in STEM offers a more efficient use of the electron dose to the sample [37]. It does that by collecting all the diffracted electrons at all q-values simultaneously while the spatial sampling is carried out by changing the position of the probe beam in a raster. Furthermore, the obtained variance in VR-FEM is generally higher than in VC-FEM, which increases the signal-to-noise ratio.

In FEM, the normalized variance V(q,R) of the diffracted intensity is calculated as a function of the scattering vector q, and the resolution R. In the case of STEM-FEM, R is the probe diameter. The brackets indicate averaging over the whole sample.

$$V(q,R) = \frac{\langle I(q,R)^2 \rangle}{\langle I(q,R) \rangle^2} - 1 \tag{2.4}$$

By scanning the sample with a MRO-sized probe, it is possible to assess the dimension of ordering. If the glass was fully featureless with complete absence of ordering at the length scale of the probe size there would be no fluctuations of the scattered intensity [3]. The presence of medium-range correlation causes anisotropy at the corresponding length scale, which allows significant fluctuation to be measured due to the different orientation

of the MRO-clusters. Fluctuations in diffracted intensity from spot to spot give rise to the FEM signal V(q,R). When the probe size has the same size as the length scale of the ordered region, the FEM signal reaches its maximum value. Figure 2.6 provides a schematic overview of the experimental setup of FEM.

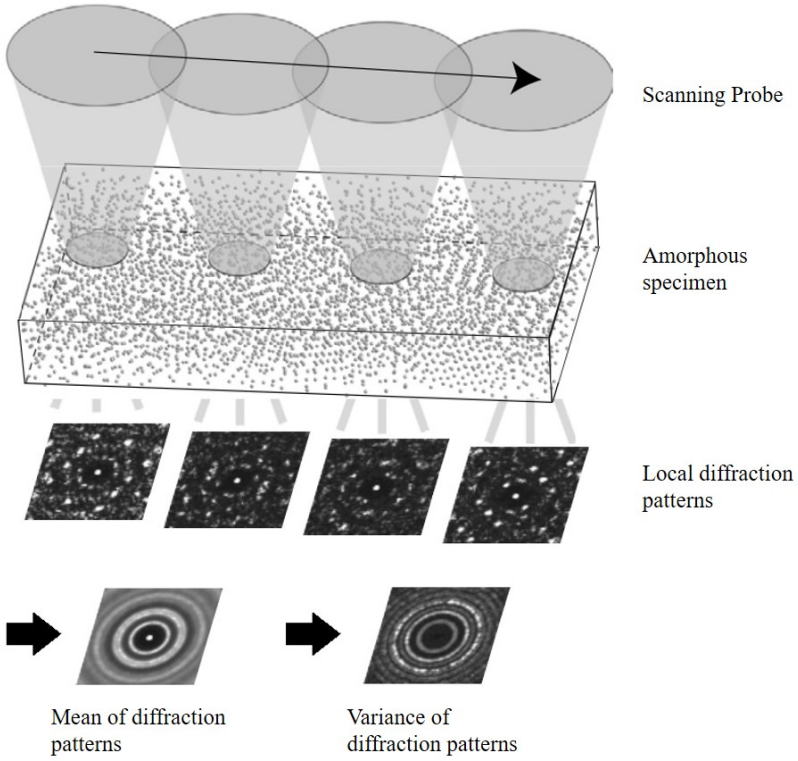

Figure 2.6: Schematics for FEM in STEM. The probe with precisely controlled size is scanned over the sample and diffraction patterns are collected at each point. From these, the mean and variance over all sample points are calculated. From: Treacy et al. (2005): Fluctuation microscopy: a probe of medium range order [36].

In VR-FEM it is required to precisely control the probe size. As FEM derives its sensitivity to MRO from coherent diffraction across the illuminated volume, a coherent probe is critical. It is the coherence length of the probe that defines the characteristic length scale of the measurement. For VR-FEM, coherent probes with a Gaussian beam profile and a FWHM between 0.5 and 5 nm are common. As the coherency is strongly related to the convergence angle, the beam must be as parallel as possible with convergence half-angles around or below 1 mrad [37]. In a STEM, at least 3 lenses are necessary to adjust R. Meeting the probe requirements with a configuration of a C1 lens, a C2 lens and an objective lens has been proven feasible on a JEOL 2010F STEM [37], but at the cost of requiring realignment and recalibration, as well as sample height adjustments for every probe size. At the *FEI Talos*, the required beam conditions could

only be achieved by using a condenser aperture of 10 µm. With a CA that small, the probe current was not sufficient.

In order to create suitable beam conditions, which are (1) a convergence angle smaller than 1 mrad, (2) full control of probe size from 0.5 nm upwards, (3) a gaussian beam profile and (4) sufficient beam current, a system with 3 full strength condenser lenses (as e.g. in an *FEI Titan*) is required [38]. Figure 2.7 shows exemplary nanodiffraction patterns at different probe sizes. It can be observed that the number of speckles increases with increasing resolution as more MRO units contribute to scattering [35] The size of the speckles are a measure of the convergence angle.

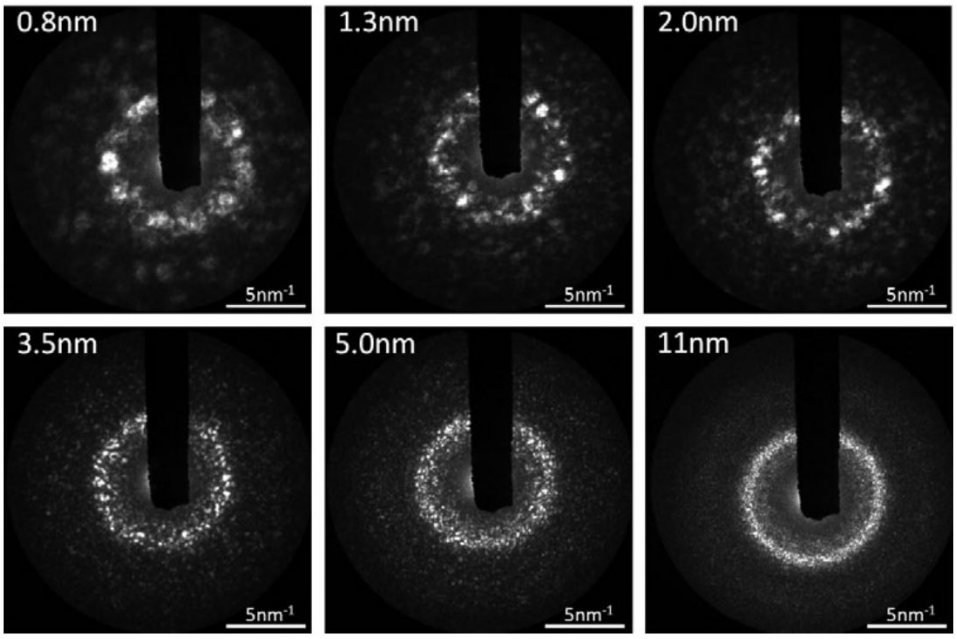

Figure 2.7: Examples of nanodiffraction patterns from different resolutions, which is indicated in the top left. The diffraction patterns have been acquired on an FEI Titan. From: Hwang et al. (2010): Variable resolution fluctuation electron microscopy on Cu-Zr metallic glass using a wide range of coherent STEM probe size.

Another aspect to consider is sample thickness. Since the diffracted intensity strongly depends on the sample thickness, even small, unavoidable variations will cause artefacts in the FEM signal, V(q,R). To remove thickness-induced artefacts a filtering method based on HAADF imaging has been developed [35]. For a homogeneous, amorphous material, the HAADF image intensity depends linearly on the thickness of the specimen. This allows for those nanodiffraction patterns which are above or below a certain threshold for thickness deviation (e.g. 5%) to be eliminated.

Calibration

This section describes the procedure attempted to implement VR-FEM on a *FEI Talos* F200X 200 kV D6312 XTwin at ScopeM. Manufacturers choose different ways to manipulate the electron beam through lenses, deflectors and apertures in different systems. Even though the fundamental operating principles are very similar in every system, this calibration procedure is tailored for the instrument mentioned above.

It is crucial to be able to precisely control the probe size while keeping the convergence angle as low as possible, maintaining maximum coherence. Following equation 2.5 the convergence angle α can be calculated from a convergent-beam electron diffraction (CBED) pattern, since the total convergence angle is proportional to the width of the diffraction disks, a(in nm^{-1}). The distance between the 000 and a hkl spot, b, is equal to the Bragg angle of that reflection $2\theta_B$, hence the pattern can be calibrated easily.

$$2\alpha = a\frac{2\theta_B}{b} \tag{2.5}$$

Another way to determine the convergence angle is presented in equation 2.6, which requires a calibrated pattern. Following the Ewald-sphere construction, the reciprocal wavelength λ is the radius of the Ewald-sphere.

$$\alpha = \arcsin\left(\frac{\lambda \cdot a}{2}\right) \tag{2.6}$$

For measuring the probe size an electropolished ultra-high purity aluminium specimen was used as a calibration standard. All real-space images of the probe were acquired at 1.05 million times magnification at 200 kV using the fluorescent screen camera (to protect the CETA-camera, which is sensitive to direct illumination). The convergent beam electron diffraction patters were also recorded on the same camera at the same voltage at a constant camera length of 520 mm.

The CBED-disks show a strong intensity drop at their edge which allowed to measure their diameter directly in the TEM Imaging and Analysis software (TIA). The probe profile has a Gaussian characteristic. Images were processed with *ImageJ*, where the intensity profile of the probe was measured. Figure 2.11 gives an example of how a probe profile for FEM should NOT look like. The profile data was imported into *Origin* where the peaks were fitted with a Gaussian curve to calculate the full width at half maximum (FWHM). Figure 2.10 shows the beam profile with a set spot size of 3 and a condenser aperture of 70 µm, resulting in a FWHM of 4.7 nm. Figure 2.9 shows probe images and the corresponding CBED-patterns Al [110], comparing them to the CBED patterns obtained in STEM mode.

Increasing the spot size number decreases the beam size by raising the current in the C1 lens. Table 2.5 shows that the probe size decreases with increasing spot size number whereas the convergence angle stays relatively constant. The decreasing convergence

angle could be a measurement artifact. At a sufficient probe current the diffraction disks show sharp edges. Since a higher spot size number significantly reduces the beam current, the diffraction disks, which do not have perfectly sharp edges, fade out, leaving the impression that they are smaller than they actually are. Figure 2.9 compares the beam characteristics of BF-mode to STEM moode. As a convergent beam technique, the diffraction disks (hence the convergence angle) are significantly larger at the same beam conditions. The convergence angle obtained in STEM mode using a condenser aperture of 70 µm is 10.41±0.22 mrad, at 10 µm 1.54±0.05 mrad.

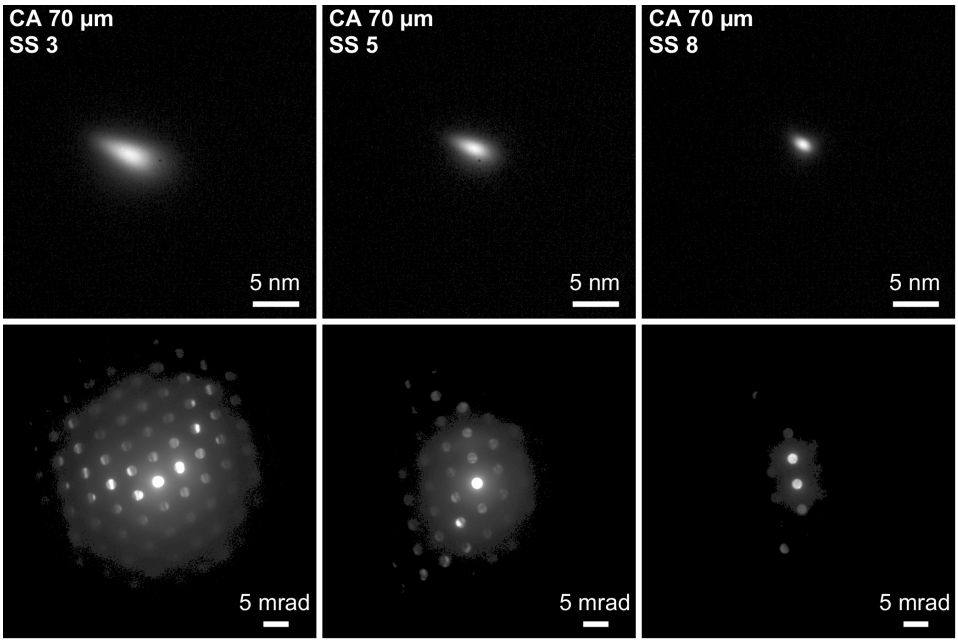

Figure 2.8: STEM probe characteristics of the *FEI Talos 200 kV*. The figure shows images of the probe with condenser aperture and spot size condition indicated in the top left corner. The corresponding CBED patterns are below. The shape of the beam could not be further improved through user alignment. Table 2.5 shows results of the probe size and convergence angle measurements.

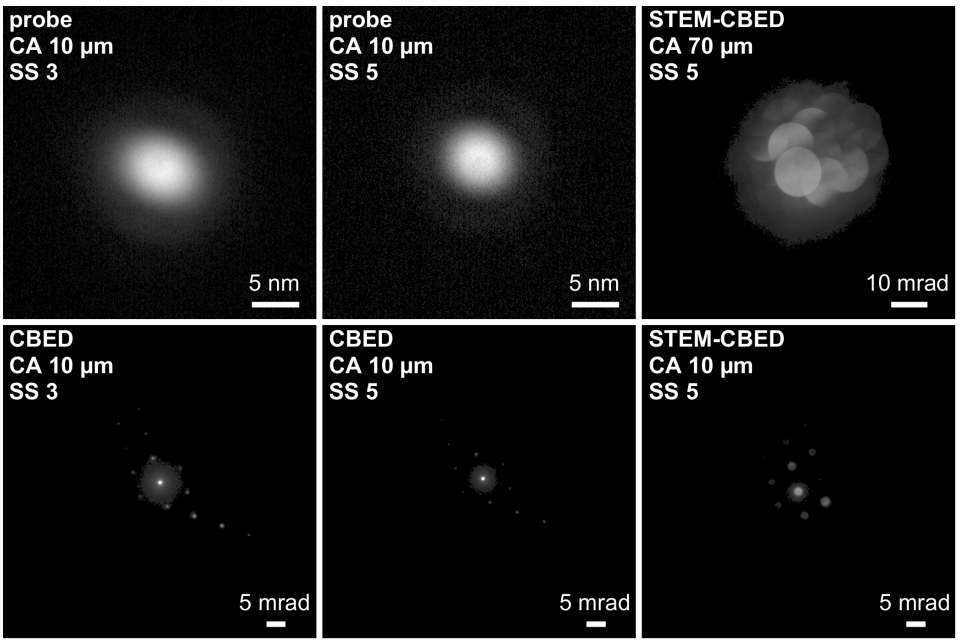

Figure 2.9: STEM probe characteristics of the *FEI Talos 200 kV*. The left four figures shows images of the probe with condenser aperture and spot size conditions indicated in the top left corner. The corresponding CBED patterns are presented below. The two images on the right show CBED patterns acquired in STEM-mode, hence the higher convergence angle.

Table 2.5: STEM probe size and convergence angle as a function of spot size number SS (variable C1-lens stength) using a constant C2 aperture of 70 µm on an *FEI Talos* at 200 kV.

	CA (µm)	SS3	SS5	SS8
probe size FWHM (nm)	70	4.7	3.1	1.6
convergence angle α (mrad)	70	70 2.19±0.04	2.13±0.07	1.98±0.03
probe size FWHM (nm)	10	7.4	6.07	/
convergence angle α (mrad)	10	0.57±0.02	0.48±0.02	/

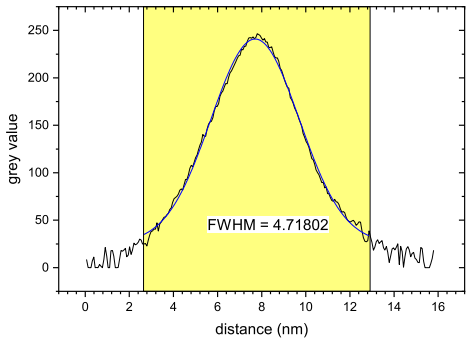

Figure 2.10: Full width half maximum of probe obtained with spot size number 3 and a condenser aperture of 70 μm in STEM mode on an *FEI Talos 200 kV*.

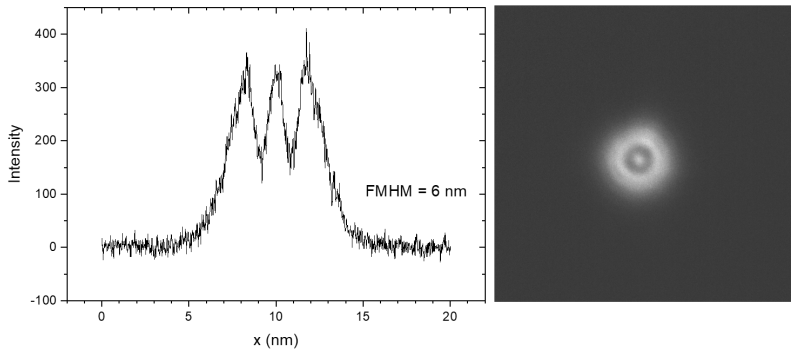

Figure 2.11: Example of how a probe profile of a FEM-probe should not look like. The picture was acquired on an *FEI Talos 200 kV*. Set spot size number was 5 and the 10 µm C2 aperture inserted.

2.4.3 EELS

Electron energy-loss spectrometry (EELS) is a transmission election microscopy technique that measures the energy distribution of electrons that have interacted with a sample. This technique is used to characterize the atomic structure and chemical composition. It can provide details on the bonding valence state, the nearest-neighbor atomic structure and the free-electron density [33]. In the present study it is used to determine the specimen thickness.

Electrons passing through a specimen interact with the atoms of the solid. While a majority of the electrons may pass without losing energy, a fraction will undergo inelastic scattering, thereby changing both their energy and momentum. Detection of scattered electrons give rise to the energy-loss signal whereas the atoms, that have undergone excitation can de-excite by emitting e.g. X-rays or Auger electrons, which can as well be processed analytically.

An EELS spectrum is usually split up into a low-loss and a high-loss region. The low-loss region contains information from weakly bound (low energy) electrons from valence- and conduction band, the high-loss region contains elemental information arising from core electrons. For a thin sample, the first peak is by far the most intense peak. It occurs at 0 eV and is called the zero-loss peak. It includes electrons that did not, or only to a small degree, undergo inelastic scattering. The width of the zero-loss peak reflects the energy spread of the electron source. Depending on the gun type, it is typically in the range of 0.2 – 2.0 eV [39].

Electron energy-loss spectrometry can be used to determine the thickness of a sample. Out of a variety of algorithms, the log-ratio method is most commonly used. The ratio of zero-loss electrons to the total transmitted electrons (elastically and inelastically scattered electrons) provides a relative measure of the specimen thickness in units of the local inelastic mean free path [40].

$$[h]\frac{t}{\lambda} = -\ln\frac{I_0}{I_{tot}} \tag{2.7}$$

In Equation 2.7 t/λ is the mean number of scattering events per incident electron. By providing the elemental composition of the sample the software simulates a mean free path λ and calculates the thickness t. Figure 2.12 shows an exemplary EELS spectrum, acquired on a *Tecnai F30*.

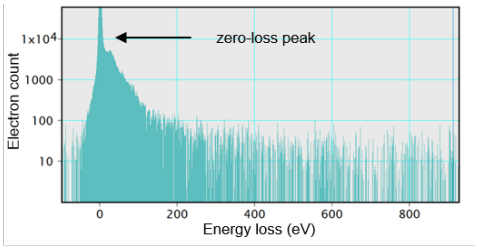

Figure 2.12: EELS spectrum of tripod polished, then ion milled Pt-Cu-P specimen, acquired on a 300 keV *Tecnai F30*. Note the large zero-loss peak (logarithmic scale).

2.5 TEM specimen preparation

Sample preparation is a critical step for TEM analysis: successful transmission electron microscopy depends highly on the quality of the specimens examined. There is a great variety of different techniques and the operator needs to choose, based on knowledge of the material properties and the analysis to be performed. When it comes to successful sample preparation, two main goals can be identified [41].

(1) *Producing an electron transparent specimen representative of the bulk material in both structure and composition.* For this, the operator needs a considerable understanding of the structure studied, in oder to identify artefacts that result from sample preparation. Knowledge of the material is critical: for example, the well-prepared operator will easily identify defects in a single crystal as artefacts. It is generally (and especially in "new", not so well-studied materials) advised to prepare a specimen by more than one method. Generally artefacts from preparation should be avoided, and since that is not always possible, it is important to identify and consider artefacts upon data evaluation.

(2) *Producing a specimen that provides access to the required information.* The ideal TEM specimen is extremely thin and should maintain constant thickness over large area together with a superb surface quality. It is flat, strong, stable under the electron beam, conducting and non-magnetic. However, different questions require different samples. The optimum thickness for dislocation measurements could be 100 nm or more whereas EELS measurements may require a thickness a tenth of that. When it comes to analyzing precipitates in a matrix: electropolishing may preferentially thin the matix, leaving the precipitates too thin to analyze whereas ion milling induces defects in the precipitates. It becomes clear that there is no such thing as an ideal sample and neither is there an ideal preparation method. A method has to be chosen carefully with respect to the analytical question for each sample.

Metallic glasses are especially prone to develop artefacts during preparation. When exposed to an energetic ion beam and/or elevated temperatures they are at risk or recrystallization. Although elaborate cooling techniques are available in both FIB and

ion milling, as the electron transparent samples are very thin, thermal conductivity is greatly reduced by geometric limitations. That means, even though the surroundings of the sample (sample holder, etc.) are at liquid nitrogen temperature, it is possible that a significant temperature gradient exists.

Electropolishing as standard preparation method was not evaluated as it has been described to produce large variations in local thickness in the sample [42]. Large thickness variations render the sample useless for fluctuation electron microscopy and produce misleading images when analyzing phase separation in metallic glasses, especially when using z- and thickness-sensitive HAADF imaging [43].

2.5.1 Ion milling

Ion milling (or ion beam thinning) is a specimen preparation method that uses bombardment with energetic Ar^+ ions to thin a sample down to electron transparency by sputtering material from the surface. Ion milling can be used without the danger of mechanically altering the material (strain hardening) regardless of the nature of the material. Unlike electropolishing, composite materials can be easily thinned. It is generally used on 3 mm disks - this geometric requirement presents one of the limitations of the method. Another risk of the method is redeposition; ejected material that is transported to another spot in the surface. Other artefacts that may arise from Ion milling include implantation of argon ions, beam-induced diffusion, thermal damage, amorphization, crystallization and others [41]. Figure 2.13 shows the schematics of an ion milling device.

It has been shown that ion milling can induce crystallization, even well below the glass transition temperature. It has been suggested that there is an energy threshold below which the structure remains unchanged under the ion beam [42]. Figure 2.14 shows that crystallization in the Cu-Zr-system can be suppressed by reducing the ion milling energy. Under the assumption that thermal effects alone are not sufficient to cause crystallization and radiation effects enhance diffusion and compositional and structural changes, it should be possible to suppress crystallization by reducing the energy and/or the milling angle. Since Pt-based glasses show extremely long milling times already at the conditions described above (heavy element) a suitable pre-thinning method has to be found. Tripod polishing (see section 2.5.2) and subsequent low-energy ion milling seems to be a promising combination.

Experimental procedures were carried out on a *Gatan PIPS II*, PIPS standing for *precision ion polishing system*. 3 mm disks were cut from the BMG rods using a *Struers Accutom* lab saw and then mechanically polished down to about 80 µm before using a dimple grinder to reduce thickness to about 20 µm. Milling parameters were set to 5 keV and 4°until the first appearance of a hole and 2 keV and 3.5°for 20 minutes afterward to improve surface quality. All procedures were carried out at liquid nitrogen temperature (-196 °C). Milling through a 20 µm sample took about 5 hours at the conditions

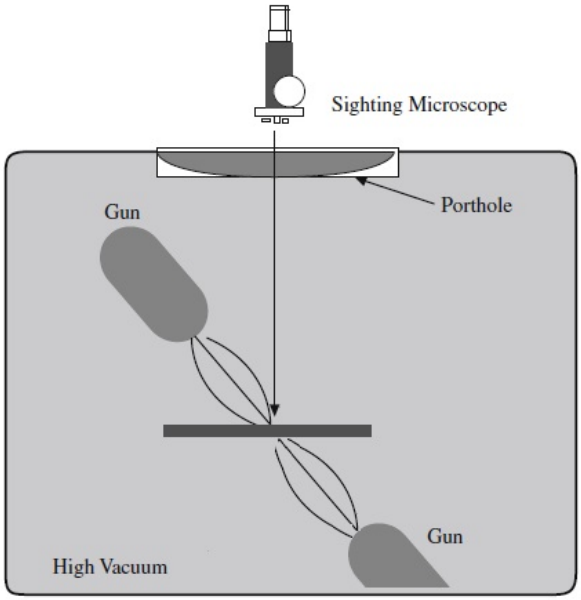

Figure 2.13: Ion milling principle: Ion guns targeting a sample that is mounted on a rotating stage in a vacuum chamber. A light microscope with an attached CCD camera is used to monitor the milling process. From: Laub, D. et al.(2010): Sample Preparation Handbook for TEM [41]

described above.

2.5.2 Tripod polishing

Tripod polishing is a mechanical sample preparation method that, using precision polishing instruments, allows to thin samples to (near) electron transparency. While some samples (like amorphous silicon) may be thinned to electron transparency through grinding and polishing alone, in other samples it allows to greatly reduce final ion milling time, thereby suppressing or greatly reducing damage induced by the ion milling. Tripod polishing yields wedge-shaped specimens with good surface quality and a very large observable area. It does, however, produce very delicate, sensitive samples that require caution upon handling.

The technique uses different devices: a rotating polisher (that allows for low rotation speeds), a sample support (the tripod) and an optical microscope that allows for constant checking of polishing quality and sample thickness (by measuring the distance between focal points). The tripod consists of a metal plate where three micrometer screws with abrasion-resistant Teflon feet allow for exact adjustment of height and angle of the sample relative to the polishing paper. The sample is glued on a piece of glass mounted on an L-shaped bracket at the bottom of the tripod. Figure 2.15 illustrates the tripod polishing process. A modified stage, as shown in (c) is not necessary with the

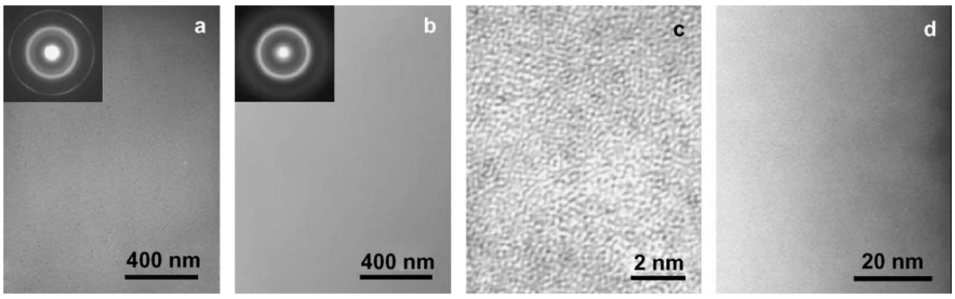

Figure 2.14: TEM-BF images and the corresponding SAED patterns of $Cu_{64.5}Zr_{35.5}$ prepared by ion milling without cooling at two different conditions: (a) 4.4 keV; (b) 3.5 keV. (c) and (d) show HRTEM- and HAADF-image, corresponding to (b). Whereas the SADP in (a) shows clear sign of crystallization, (b) is fully amorphous. From: Sun, B. et al. (2005): Artefacts induced in metallic glasses during TEM sample preparation [42].

newest generation of tripods[2].

Polishing is performed on diamond-embedded plastic disks with decreasing grain sizes (30, 15, 6, 3, 1, 0.5, 0.1 µm) on a rotating disk while sticking to a strict protocol of thicknesses-to-be-achieved and rotation speeds for each step. [41] As a first step, an approximately 300 µm thick disk is cut from the sample and glued on the glass part. After one side is polished perfectly flat, the specimen is flipped and, after the micrometer screws have been adjusted to the desired angle, the same polishing routine is repeated on the other side. After the specimen is unglued from the bracket, it is cleaned in acetone and glued onto a TEM ring-support. This step has to be carried out with great caution.

The sample discussed in this study, $Pt_{57}Cu_{23}P_0$ was prepared at the *Centre Interdisciplinaire de Microscopie Electronique (CiMe), EPFL*. After polishing, the sample was ion milled to electron transparency using the following routine: (1) 7 hours, 1 keV. (2) 1 hour, 0.5 keV. (3) 1 hour, 0.2 keV. Gun angles were always set to 5 °(top) and 6 °(bottom). The rotation speed was set to 2 rounds per minute; milling was performed at liquid nitrogen temperature. Figure 2.16 shows images of both an unsuccessful and a successful sample preparation.

[2]Allied High Tech: http://www.alliedhightech.com/Equipment/tem-wedge-polisher, February 2018

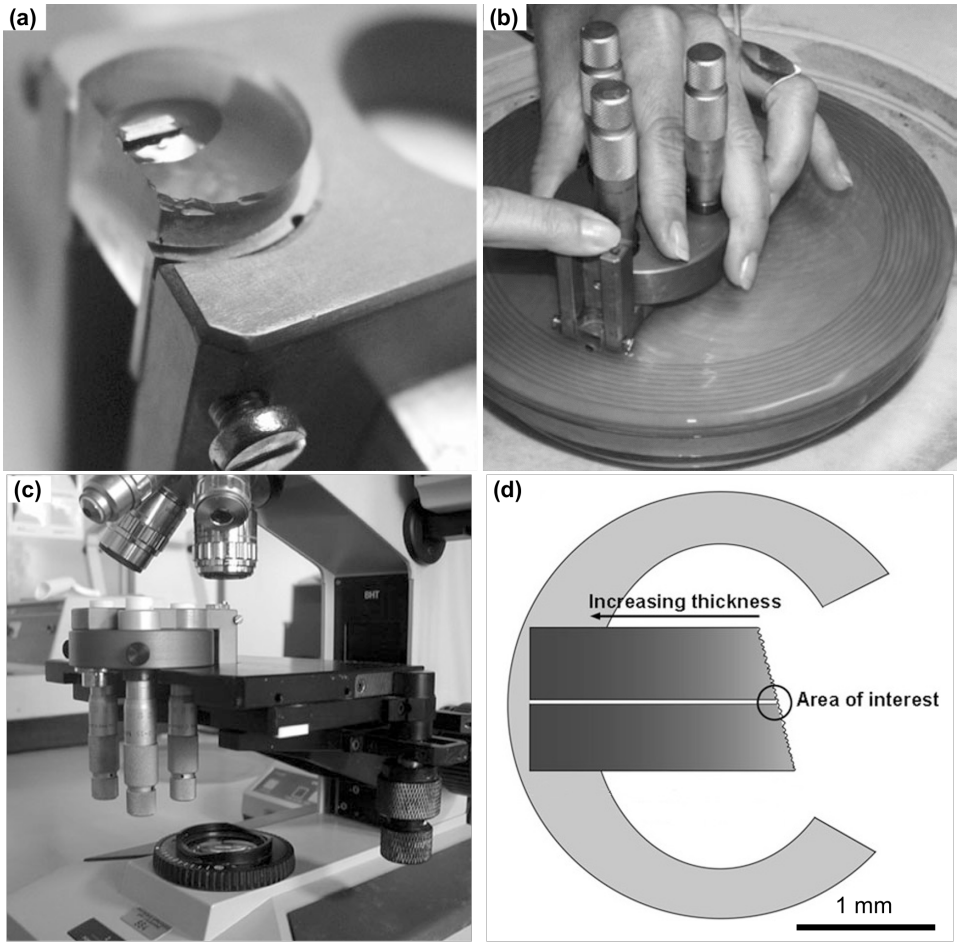

Figure 2.15: (a) sample glued to a super-flat glass cylinder on the L-shaped bracket of the tripod. (b) polishing is a manual process: tripod with micrometer screws on the rotating polisher. (c) microscope with modified stage for checking polishing quality and sample thickness. (d) top-on view of a cross-sectional composite sample mounted on the support, ready for TEM observation. Adjusted and compiled from: Laub, D. et al.(2010): Sample Preparation Handbook for TEM [41].

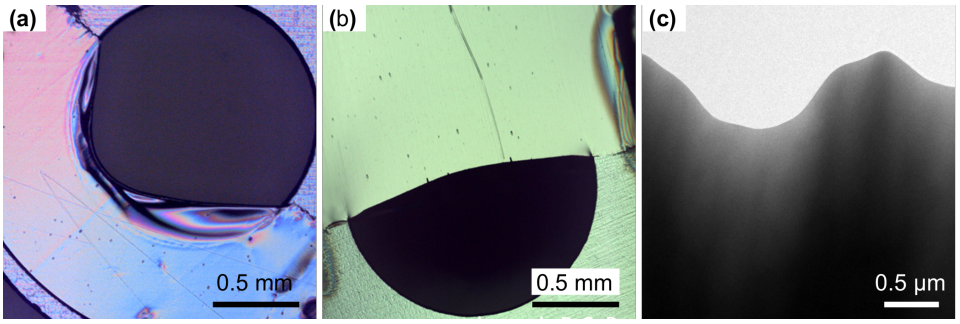

Figure 2.16: Tripod polished Pt-Cu-P BMG samples after ion milling finish: The specimen in (a) is badly damaged due to a short overload in the PIPS and cannot be observed in the TEM as the electron transparent region is missing. This illustrates the sensitivity of a tripod polished specimen. The other pictures show the result of a successful sample preparation: under the light microscope (b) and in the TEM (c).

2.5.3 Ultramicrotomy

Ultramicrotomy is a mechanical sample preparation where specimens are produced by cutting them directly into electron transparent ultra thin slices. It enables to produce constant thickness sections in the range of 30-150 nm by cutting the material with a diamond- or glass knife. This is roughly the equivalent of cutting a 0.1 mm-thick human hair into up to 2000 slices along its diameter [44]. Ultramicrotomy is a well established technique in biology, but has gained increasing attention in the materials science community especially for nanocrystalline materials [45].

Ultramicrotomy produces samples with extensive electron-transparent regions of uniform thickness without beam damage. Typical artefacts are knife marks and tearing. The operator has to be aware of possible thermal damage through frictional heating and shearing. The technique uses an instrument called an ultramicrotome which is equipped with a knife support, a goniometer system, a precision knife and a light microscope. As shown in figure 2.17, the sample is attached to an arm that guides it to the knife and advances incrementally to produce a large number of constant-thickness sections. Depending on the material, samples can be embedded into a resin or cut directly without embedding.

The samples prepared in this study have been milled down to 20 µm thickness and cut into approximately 0.5 mm wide strips prior to embedding in *Epoxy Embedding Medium* 49345 F. To harden the polymer, the embedded samples were placed into an oven at 60 °C for 24 hours. Figure 2.18 shows an exemplary Pt-Cu-P BMG specimen on a carbon grid.

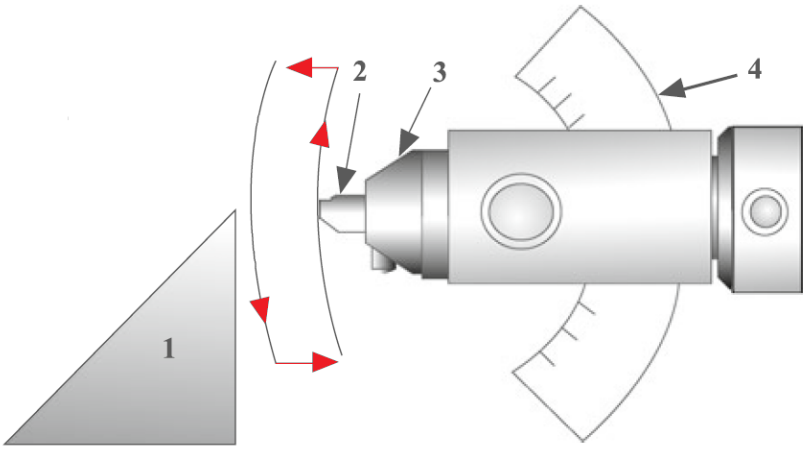

Figure 2.17: Schematic of an ultramicrotome arm, goniometer and knife configuration: (1) knife. (2) sample. (3) sample holder. (4) goniometer. The red arrows indicate the sample holder trajectory. Ajusted from: Laub, D. et al.(2010): Sample Preparation Handbook for TEM [41]

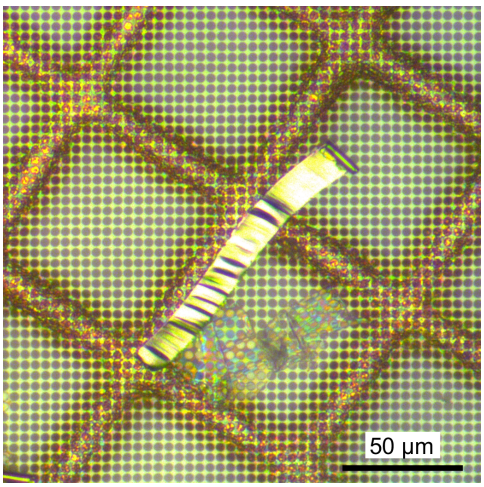

Figure 2.18: A section of Pt-Cu-P BMG on a carbon grid.

2.5.4 FIB

The focused ion beam (FIB) technique is used to produce electron transparent specimens by cutting thin slices (lamellas) from precicely defined regions of a sample. It uses an energetic beam of focused ions (most commonly Ga^+) whose energy can be varied over a wide energy range.

After selecting the area of interest, using a CVD process, a carbon film is deposited on top of what will be the specimen as a protection layer. In the next step, two course trenches are cut on both sides of the sample area. The following fine cuts, where the current is reduced from about 30 nA to 3 nA at 30 kV, are performed to reduce the influences of beam damage within the specimen. The subsequent side- and bottom-cuts leave the lamella attached to the bulk at only a very small link. At this point, a micro manipulator controlled needle is "welded" to the lamella before the connection between the lamella and the bulk is capped completely. After lift-out, the lamella is attached to an omniprobe TEM half-grid. Then, the lamella is polished and thinned further with decreasing currents, finishing with a low-kV (5 kV) showering.

In the present study, FIB was primarily used to prepare TEM specimens from samples of recrystallized BMGs. The small samples (approx. 10 mg, 1 mm spheres) were embedded in Bakelite and polished to reveal its micro structure. Only FIB allows to precisely choose a region of interest that would later be used to perform electron diffraction on the different phases for identification. Both figures 3.20 and 3.24 show electron micrographs of TEM specimens prepared by FIB.

2.5.5 Plasma cleaning of specimens

As a standard routine prior to characterization in the TEM, samples have been cleaned with a *JEOL EC-52000IC Ion Cleaner*. It operates at a pressure of about 40 Pa with

a 310 V glow discharge plasma on a carbon target. Recommended cleaning time is 5 min.

An ion cleaner holds a specimen and the holder under a glow discharge in order to remove residual (organic, usually hydrocarbons) material, which can arise from either pretreatment of the sample or sample storage. Removing these contaminants prevents specimen contamination which arise due to polymerization of hydrocarbons upon irradiation with an electron beam in the microscope. However once contamination has occurred, the plasma cleaner cannot remove it; the sample has to be ion milled or cleaned in a FIB. Figure 2.19 illustrates the importance of avoiding contamination.

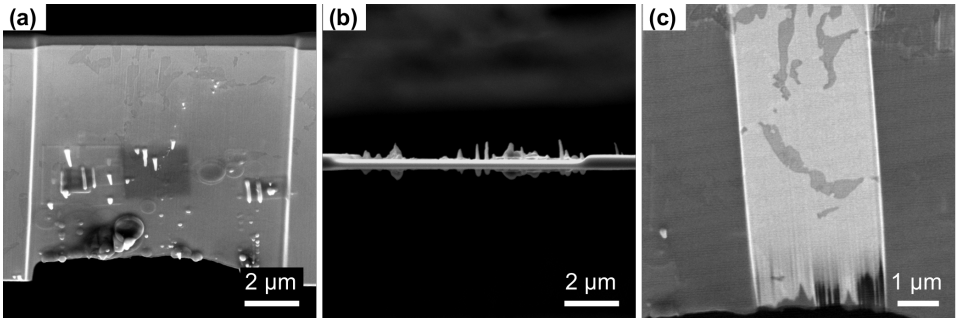

Figure 2.19: Secondary electron images of a FIB-lamella that has not been plasma-cleaned prior to TEM analysis. Severe carbon contamination in front (a) and side-on view (b). (c) shows the same area after clean-cutting and thinning in the FIB.

2.6 Analysis software

Very often the researcher relies greatly on the pioneering work of others who have identified a problem and tackled it by writing an appropriate program. During this work, especially for processing and indexing diffraction patterns, a number of existing programs have proven very helpful.

Whenever an "azimuthal-" or "rotational average" is mentioned, it has been calculated from the (amorphous) diffraction patterns using *eRDF Analyser* by J. Shanmugam and others [29]. Designed Matlab GUI for calculation of the reduced density function, it was used to calculate the azimuthally averaged intensity curves as functions of the scattering vector q.

For indexing diffraction patterns for phase analysis, two programs have been used. One on which was *diffractGUI*, part of the software suite *CrysTBox* by M. Klinger [46]. It allows for automated processing of both spot and disc diffraction patterns. For many patterns (those that show intense, sharp spots) the software is able to fit a regular lattice following a RANSAC (random sample consensus) algorithm. For more complex patterns, it allows for manual marking of spots. Provided crystal data in the form of

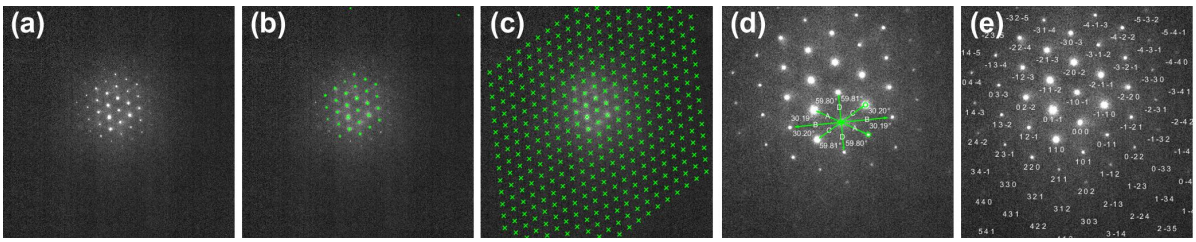

Figure 2.20: (a) a selected area diffraction pattern from a region. Assumption phase is PtP_2 needs verification (b) automatic detection of the strongest spots (c) a RANSAC algorithm fits a regular reciprocal lattice to the set of strongest detected spots (d) several vectors are localized in the regular lattice, d-spacings and angles are compared to different zone-axis patterns (e) the pattern matches with the [111] zone axis pattern of PtP_2.

a crystallographic information file (.cif, can be either created or downloaded from any crystallographic database, given that the crystal structure is known) it simulates patterns from that structure and compares them to the experimental pattern. After that, it provides a quantitative evaluation of the best fit in terms of angular- and d-spacing deviation. Figure 2.20 illustrates the process of indexing and matching a diffraction pattern using diffractGUI. Despite requiring manual intervention, for more complex patterns and weak spots, the software *Single Crystal* a part of the *Crystal Maker* package, proved more appropriate and was therefore used as well.

3 Results

3.1 XRD measurements

Due to the q-space limitation, the obtained X-ray diffraction data does not allow to calculate a radial distribution function. It can, however, provide other useful information. The absence of sharp peaks does not allow to distinguish between nanocrystalline or amorphous state, but allows to exclude the possibility of larger crystalline domains in the sample. Evaluating the XRD-patterns in figure 3.1 provided no indication to assume the sample would not be amorphous.

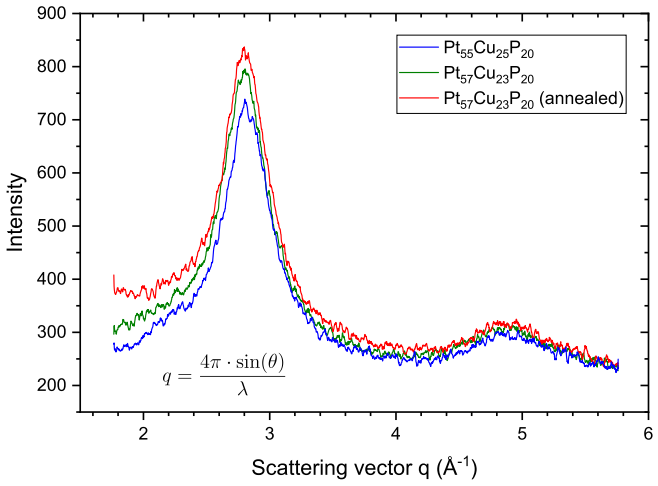

Figure 3.1: XRD patterns of amorphous PtCuP-alloys with different compositions. Typically for amorphous materials, all of them show wide diffraction maxima and absence of sharp Bragg peaks. The curve has been smoothened with a binning of 5.

The *Ehrenfest formula* (equation 3.1) can be derived from the Debye formula, which describes the scattered intensity as a function of the scattering vector, depending on the total number of pairs of identical atoms seperated by the same distance and the total number of scattering atoms [1]. The Ehrenfest formula yields a characteristic relation a, which is the most probable distance between two atoms. These values are summarized in table 3.1.

$$q_{max} = 1.23 \cdot \frac{2\pi}{a} \tag{3.1}$$

Table 3.1: XRD derived q-values of the first maximum and resulting values for a, the most probable distance between two atoms. It can be seen that the value for $Pt_{55}Cu_{23}P_{20}$ differs slightly from the other sample, but the deviations are very small.

Sample	q_{max} (Å^{-1})	a (Å)
$Pt_{55}Cu_{25}P_{20}$	2.8201±0.0005	2.7404±0.0004
$Pt_{57}Cu_{23}P_{20}$	2.7992±0.0004	2.7609±0.0004
$Pt_{57}Cu_{23}P_{20}$ annealed	2.8040±0.0003	2.7561±0.0004

3.2 Composition analysis

Only one sample with the provided nominal composition $Pt_{55}Cu_{25}P_{20}$, which had been recrystallized during a DSC run, could be successfully dissolved in acqua regia and was therefore accessible for analysis. Table 3.2 gives an overview on measuring parameters and measured composition.

Table 3.2: Results of ICP-OES measurement of $Pt_{55}Cu_{25}P_{20}$

Analyte	wavelength (nm)	concentration (mg/l)
Pt	214.424	7.98
Cu	327.395	1.22
P	214.914	0.45

At an initial total analyte concentration of 10 mg/l compared to a measured 9.67 mg/l, a relative error of 3 % should be considered. Taking into account the individual atomic masses, the nominal composition can be calculated as $Pt_{54.7}Cu_{25.8}P_{19.5}$. Table 3.3 compares the given composition to the results of ICP-OES- and EDS-measurements. It can be seen that the EDS measurements are highly inaccurate while there is no reason to assume that the provided compositions are not correct. The same applies to the $Pt_{57}Cu_{23}P_{20}$ sample: although there is no ICP-OES data, comparing only the EDS data, the $Pt_{57}Cu_{23}P_{20}$ sample shows elevated Pt-concentrations, reduced Cu-concentrations, while P stays about the same.

To verify the homogeneous and featureless characteristic of the material, a chemical mapping was performed using STEM-EDS. Additionally, a local electrode atomprobe measurement was carried out. Figure 3.2 illustrates the homogeneous nature of the provided $Pt_{57}Cu_{23}P_{20}$ sample. Both a 3-D atomprobe reconstruction and a chemical map obtained by STEM-EDS do not show any hint of structural correlation or precipitates.

Table 3.3: Comparison of the provided composition and the results of ICP-OES measurements (3 % rel. error) and EDS (assuming 10 % rel. error) of the $Pt_{55}Cu_{25}P_{20}$ sample, all in atomic percent. The right column shows the EDS results of the $Pt_{57}Cu_{23}P_{20}$ sample obtained in an SEM.

Element	provided	ICP-OES	EDS (Pt_{55})	EDS (Pt_{57})
Pt	55	54.7 ± 1.6	66.1 ± 6.6	68.0 ± 6.8
Cu	25	25.8 ± 0.7	23.2 ± 2.3	20.9 ± 2.1
P	20	19.5 ± 0.6	10.7 ± 1.1	11.2 ± 1.1

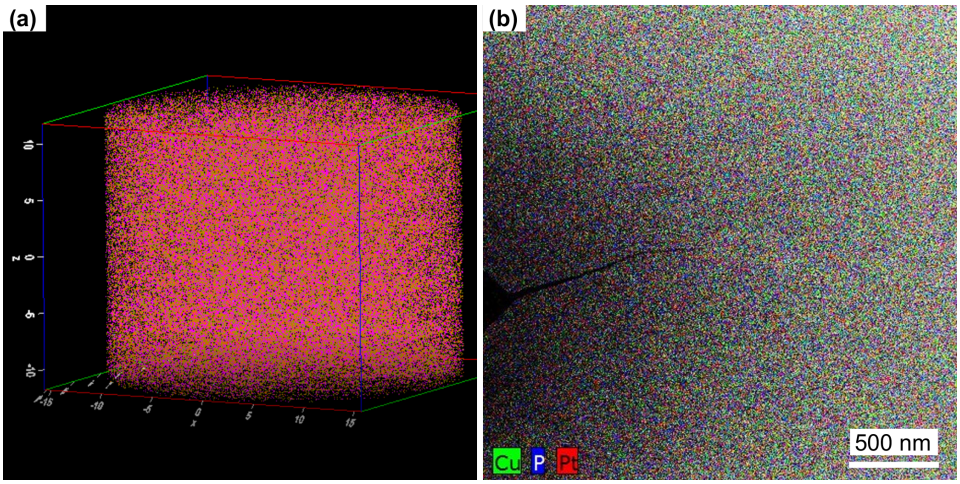

Figure 3.2: The $Pt_{57}Cu_{23}P_{20}$ sample is fully homogeneous and does not show any precipitates. (a) 3-D reconstruction of an local electrode atomprobe measurement with ca. 400000 ranged atoms acquired on a *Cameca LEAP 4000X-HR* (b) chemical map acquired by STEM-EDS on an *FEI Talos 200 kV*.

3.3 Thermophysical properties

3.3.1 Calorimetric studies

The glass transition temperature T_g and the onset temperatures for crystallization T_x and melting T_m have been determined in a series of DSC experiments. Figure 3.3 shows one exemplary curve for each material. Table 3.4 presents the calibration-corrected values for the glass transition temperature, T_g, the onset temperatures for crystallization and melting, T_x and T_m, and the extent of the supercooled liquid region $\Delta T_x = T_x - T_g$.

In figure 3.3, the points (1), (2) and (3) depict temperatures, from which material was quenched. These samples, which had a mass of approximately 10 mg each, were metallographically prepared; that means embedded and polished, hence prepared for SEM analysis. For (1), the sample was quenched from 312 °C, halfway through the crystallization peak. For (2), the sample was quenched after crystallization at 400 °C

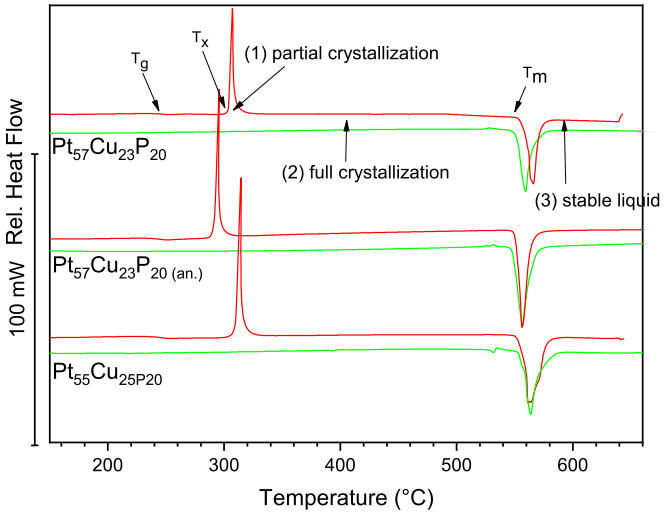

Figure 3.3: DSC curves of the different Pt-Cu-P samples with the first heating curve (in red) showing a glass transition at T_g, a crystallization peak at T_x and a melting peak at T_m. The second heating curve (in green) shows only a melting peak as the material is fully crystalline after the first cycle. The points (1), (2) and (3) depict temperatures, from which material was quenched for phase analysis.

and for (3), the sample was quenched from the stable liquid at 650 °C. Figure 3.4 shows back-scatter electron micrographs of the different phases.

Each of the different phases in figure 3.4 is labeled with A, B, C or D. These labels correspond to different compositions, plotted in the ternary phase diagrams displayed in the figures 3.5 and 3.6. It can be observed that for the sample that had not been heated to melt the compositions of the different phases do not deviate greatly from the general composition of the alloy. For those samples that had been heated above the melting temperature a much larger deviation of the individual composition of the phases from the general alloy composition can be observed. The PtP_2 phase only occurs upon crystallization from the stable liquid.

Table 3.4: Results of the DSC measurements of the different PtCuP BMGs. The table shows the calibration-corrected values for the glass transition temperature, T_g, the onset temperatures for crystallization and melting, T_x and T_m, and the extent of the supercooled liquid area $\Delta T_x = T_x - T_g$.

sample	T_g (°C)	T_x (°C)	T_m (°C)	ΔT_x (°C)
$Pt_{55}Cu_{25}P_{20}$	236.6 ± 1.8	309.8 ± 0.2	553.8 ± 2.1	73.2 ± 6.8
$Pt_{57}Cu_{23}P_{20}$	237.0 ± 0.9	303.4 ± 0.3	551.4 ± 2.0	66.5 ± 2.1
$Pt_{57}Cu_{23}P_{20}$ (an.)	236.7	292.0	550.1	55.3

Table 3.5: Comparison of total enthalpy of fusion H_m of the fully amorphous samples in the first run and the recrystallized material in the subsequent heating cycles. An increase in H_m by almost 10% can be observed for each sample.

Sample	Hm (J/g, first heating)	Hm (J/g, subsequent heatings)
$Pt_{55}Cu_{25}P_{20}$	76.9 ± 0.8	83.7 ± 1.2
$Pt_{57}Cu_{23}P_{20}$	74.8 ± 2.9	79.0 ± 1.7
$Pt_{57}Cu_{23}P_{20}$ (an.)	76.0	80.7

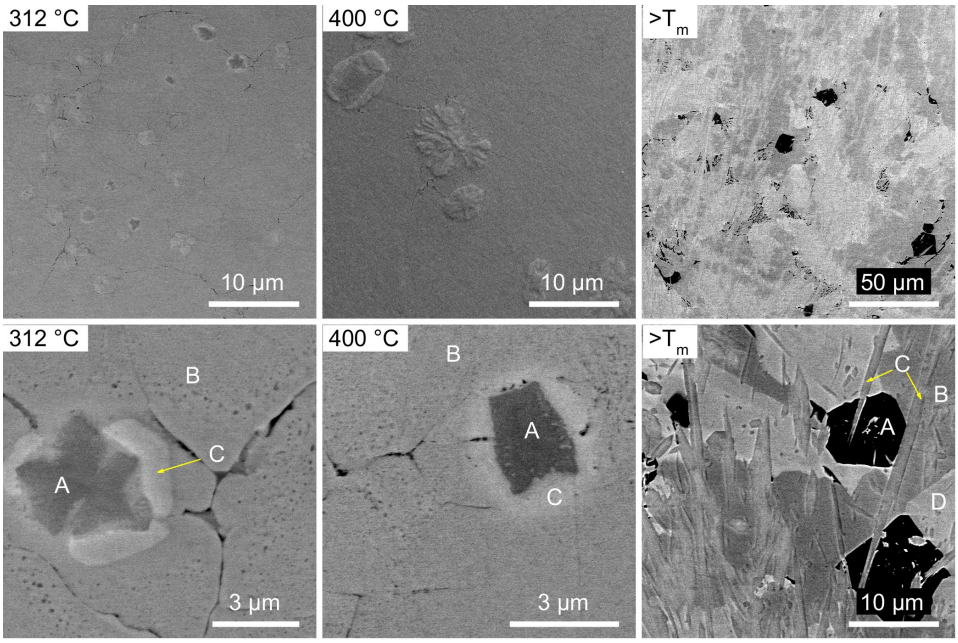

Figure 3.4: SEM images of recrystallized $Pt_{57}Cu_{23}P_{20}$ samples, acquired on a *Hitachi SU70* in BSE mode and 20 kV. The temperatures, from which the samples had previously been quenched in the DSC, are indicated at the top left of each image.

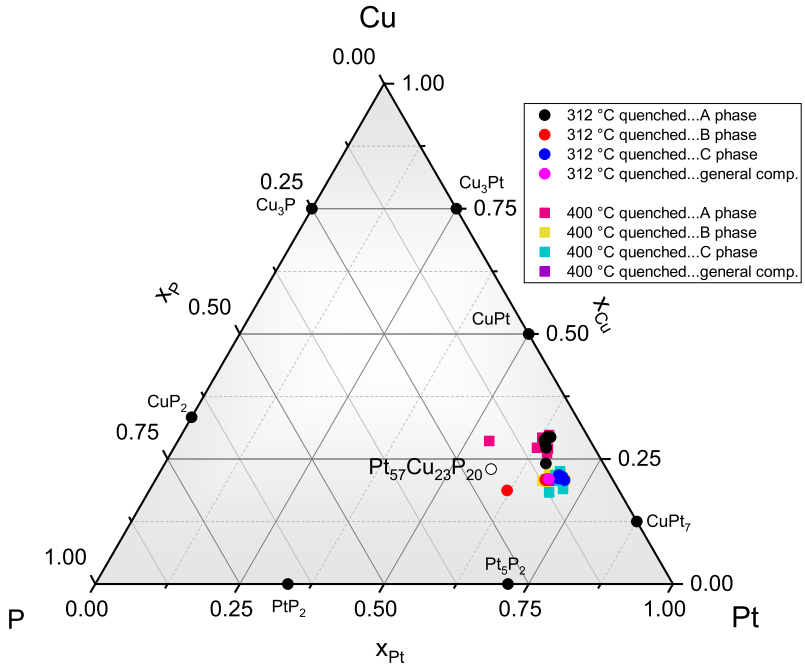

Figure 3.5: Ternary phase diagram showing the compositions of the different phases that occur upon crystallization of $Pt_{57}Cu_{23}P_{20}$ as measured with SEM-EDS. One sample (312 °C) was heated halfway through the crystallization peak and then quenched, the other one (400 °C) was quenched after full crystallization. It can be seen that that the spots, indicating the compositions of the different phases are concentrated in an area around the general composition of the alloy.

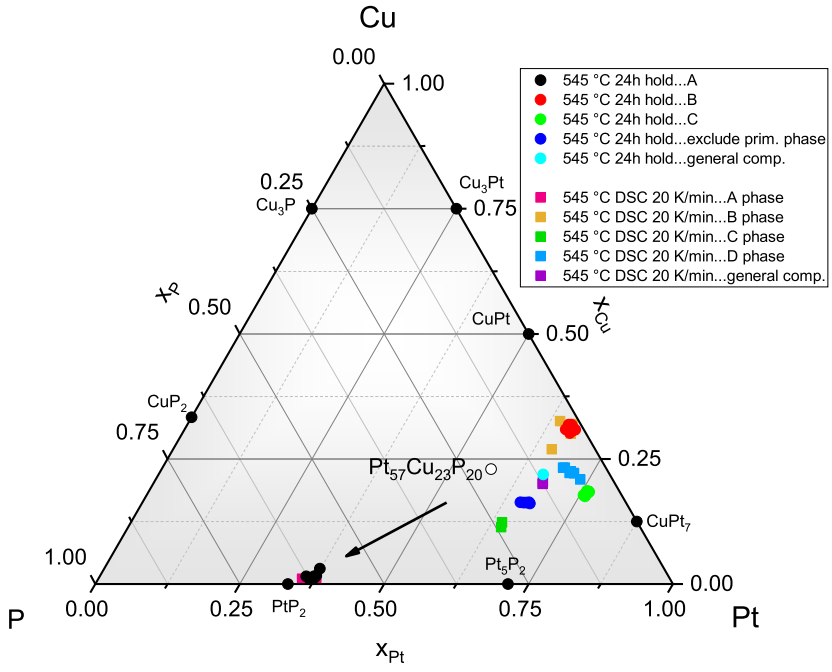

Figure 3.6: Ternary phase diagram showing the compositions of the different phases that occur upon crystallization of $Pt_{57}Cu_{23}P_{20}$ as measured with SEM-EDS. The same limitations in measurement accuracy as discussed in section 2.3 apply. Other than the samples shown in figure 3.5, these samples were heated to melt and crystallized from the stable liquid. It can be seen that the spots, indicating the compositions of the different phases, are spread out over a wide area around the general composition of the alloy.

3.3.2 Determination of the critical cooling rate

The critical cooling rate R_c of the eutectic $Pt_{57}Cu_{23}P_{20}$ sample was experimentally determined in a series of FDSC measurements. Three selected experiments are presented below: One to determine the R_c, one for the critical heating rate and one to see if R_c could be recovered after the thermal cycles.

Looking at figure 3.7 one can see that the first crystallization peak occurs at a rate -3 Ks^{-1}. The critical cooling rate is therefore (until further refinement) -4 Ks^{-1}. Figure 3.8 shows the subsequent heating curves following the cooling curves, an overview on the crystallization behavior (prenuclei forming at lower cooling rates facilitating crystallization upon heating) is provided in 3.6.

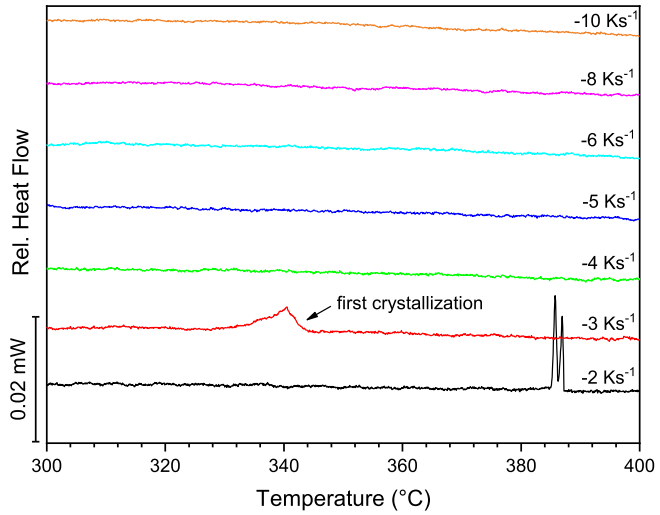

Figure 3.7: FDSC measurements of $Pt_{57}Cu_{23}P_{20}$. Varying cooling rates to determine the critical cooling rate. Crystallization occurs below -4 Ks^{-1}.

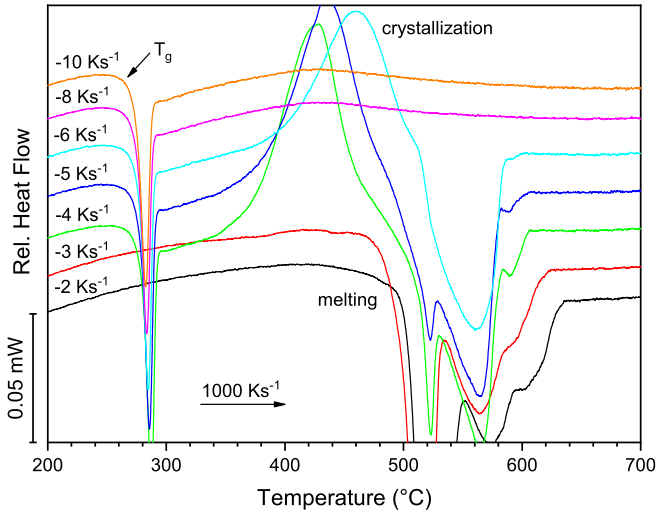

Figure 3.8: FDSC measurements of $Pt_{57}Cu_{23}P_{20}$. Consecutive heating curves (1000 Ks^{-1}) with previous cooling rates indicated on the left. Crystallization upon heating could not be bypassed for cooling rates of -6 Ks^{-1} or lower. Heating curves after cooling at rates lower than -4 Ks^{-1} (critical cooling rate) show no glass transition.

Table 3.6: Crystallization behavior of $Pt_{57}Cu_{23}P_{20}$ as derived from FDSC measurements at a constant heating rate:

Cooling rate (Ks^{-1})	crystallization behavior
..., -2, -3	no glass transition, no crystallization
-4, -5, -6	crystallization without bypass
-8, -10, ...	bypass of crystallization

A more reliable criterion for the observation of a glass transition in FDSC than the exothermic crystallization peak on a cooling curve is presented in figure 3.9. With the appearance of the first crystalline phase the difference in heat capacity Δc_p between the glassy and the supercooled liquid state disappears. The heating curve following cooling at the critical cooling rate shows the glass transition of a fully amorphous material and therefore is the last curve not to show a reduced Δc_p.

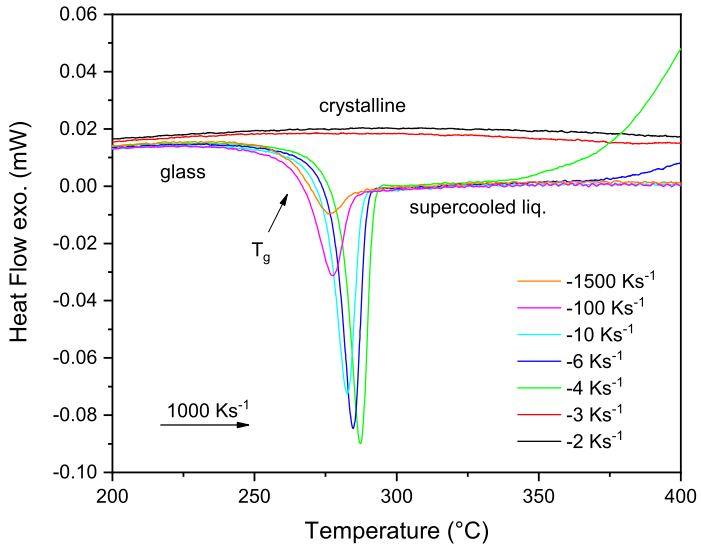

Figure 3.9: FDSC measurements of $Pt_{57}Cu_{23}P_{20}$. Heating curves at 1000 Ks^{-1}. Presence of a crystalline phase leads to a reduction of the heat capacity difference.

Following the experiments to determine the critical cooling rate, experiments to find the critical heating rate (at which crystallization upon heating is bypassed) have been conducted. Therefore the cooling rate was set at a constant -1000 Ks^{-1} and the heating rate was varied for each cycle. Following the results of the R_c measurements displayed in figure 3.8 one would expect the critical heating rate to be below 1000 Ks^{-1}. Figure 3.10 shows the heating curves, which display a crystallization event at all rates. Also the subsequent coolings in figure 3.11 (at -1000 Ks^{-1}) now show a crystallization peak, indicating that the critical cooling rate is now greater than 1000 Ks^{-1}.

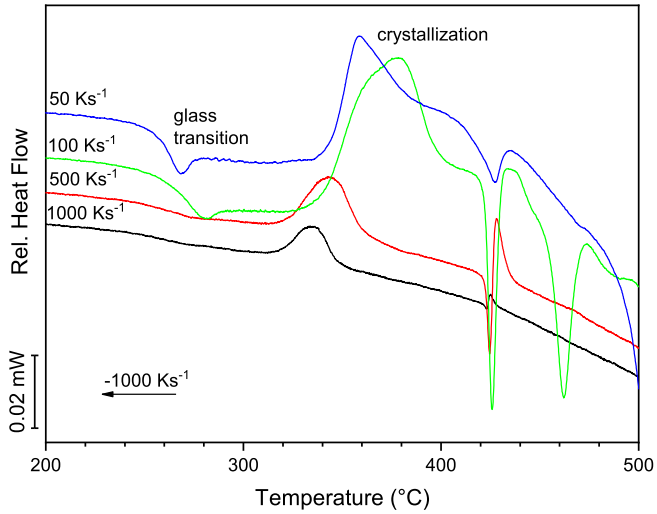

Figure 3.10: FDSC measurements of $Pt_{57}Cu_{23}P_{20}$. Critical heating rate (at a constant cooling rate of 1000 Ks^{-1}) could not be determined as a crystallization peak was observed for every rate.

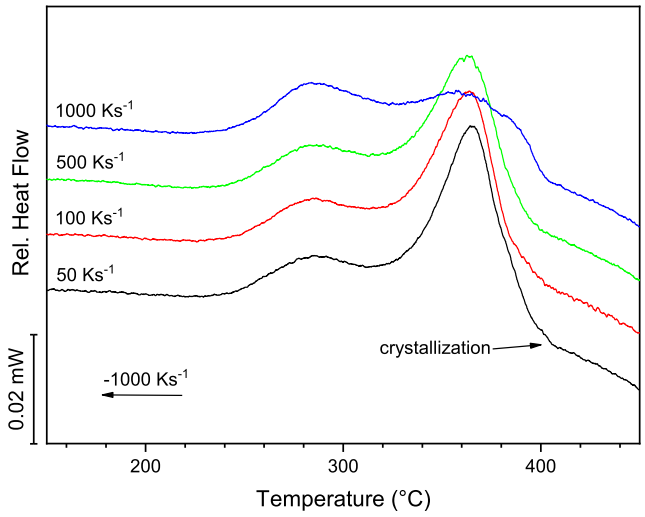

Figure 3.11: FDSC measurements of $Pt_{57}Cu_{23}P_{20}$. Subsequent cooling rates at a constant -1000 Ks^{-1} with prior heating rates indicated left on the top of every curve. The critical cooling rate could not be recovered.

The next experiment was set up to determine R_c following the previous thermal cycles. Figure 3.12 shows that the critical cooling rate has increased to -3000 Ks^{-1}. Figure 3.13 indicates that crystallization upon heating could not be bypassed for any cooling rates.

Further experiments, which included thermal cycling and isothermal holdings below and above T_m with the objective to erase the thermal history of the sample, did not allow to recover the initial R_c.

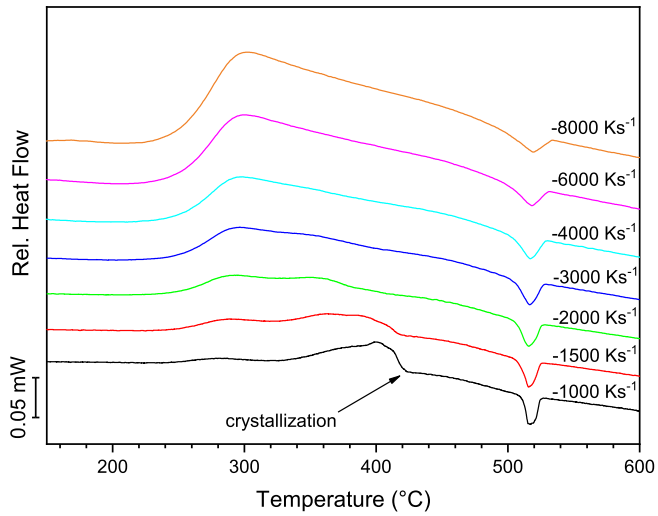

Figure 3.12: FDSC measurements of $Pt_{57}Cu_{23}P_{20}$. Cooling curves at a constant heating rate of 100 Ks^{-1}. The critical cooling rate has increased from -4 Ks^{-1} to 3000 Ks^{-1}

The heating curves in figure 3.13 show a complicated system of metastable phases with major melting events at 420 °C and 510 °C.

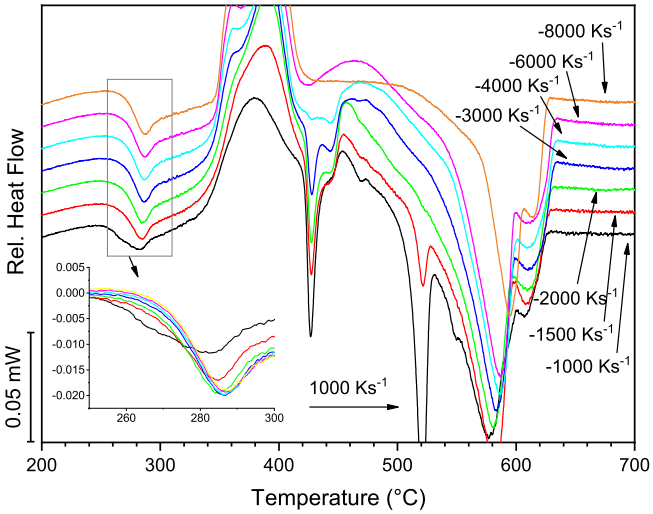

Figure 3.13: FDSC measurements of $Pt_{57}Cu_{23}P_{20}$. Consecutive heating curves (1000 Ks^{-1}) with previous cooling rates indicated on the right. Crystallization upon heating could not be bypassed for any cooling rates. The inset graph shows the decrease in Δc_p for lower cooling rates.

3.4 TEM specimen preparation

Having tried different preparation routines, it was important to develop a procedure on how to evaluate the individual methods in terms of the potential recrystallization they may have induced. For this purpose, diffraction patterns were acquired at different thicknesses. The ratio of the amorphous to crystalline peak intensity, which changes with increasing thickness, was then quantified. This allows to differentiate between such crystallization as a material property and such that has been induced by sample preparation, thus distinguishing bulk from surface crystallization.

All SAPDs have to be aquired at identical illumination conditions. This means spot size, apertures, intensities, exposure times, etc. have to be kept constant. To define the right setting, a condition, which does not saturate the camera at the very edge (thin area) but still provides some signal in thick areas (where the diffracted beam becomes blurred and the diffuse background is getting bright), had to be found. Starting from the very edge of the sample (hole), a number of equally spaced regions were selected for acquisition of selected area diffraction patterns. Thickness was measured using the EELS log-ratio (relative) method. In the next step, the image data was loaded into *eRDF-Analyser* [29] to calculate the azimuthal averages, which were then plotted against the thickness.

3.4.1 Ion milling

Ion milling in the *Gatan PIPS II* produces specimens from 3 mm disks that have a smooth surface and wide observable (electron transparent) regions around the hole. All specimens showed both characteristic diffuse amorphous rings and discrete diffraction spots that resulted from a crystalline fraction in the material. Figure 3.14 shows a bright field image of the observable region around the hole. The different sites, from where SADPs have been recorded, are marked with red crosses. The exemplary display of four diffraction patterns shows that even in relatively thick areas the spots arising from diffraction from crystalline material are still clearly visible. It appears that the crystalline fraction, following the described procedure is present throughout the bulk of the material.

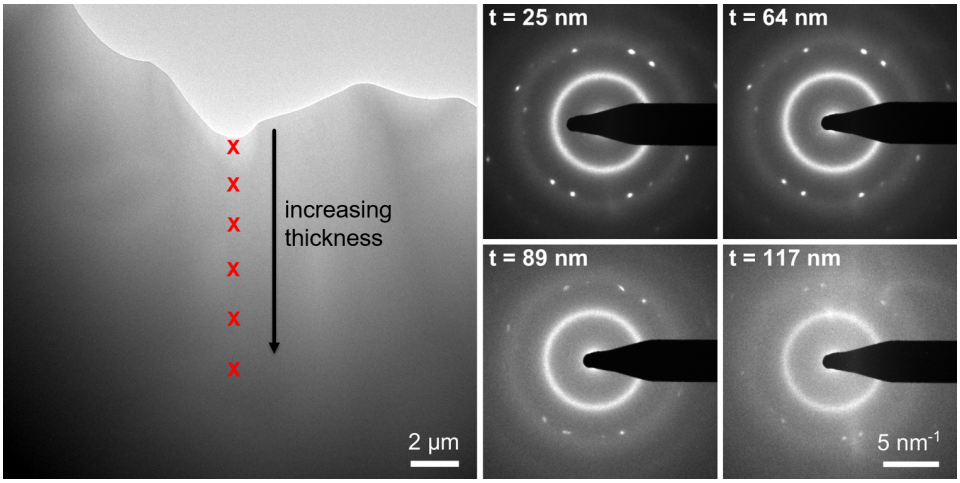

Figure 3.14: Left: TEM-BF image of edge of the Pt-Cu-P BMG specimen produced by ion milling. right: exemplary SADPs showing both crystalline spots and amorphous rings, acquired at different thicknesses (indicated in BF-image).

3.4.2 Tripod polishing

To evaluate the quality of the tripod polished specimen, the routine described in section 3.4 was carried out. Selected area diffraction patterns were acquired at different thicknesses and the thickness measured using EELS. Figure 3.15 shows six exemplary diffraction patterns at increasing thicknesses. One can clearly see that the spots, which arise from diffraction at crystalline material, become less dominant in thicker regions and fade out faster than the amorphous rings. Figure 3.16, which shows a 3-D plot of the azimuthal averages obtained from the SADPs, encourages this perception. It can be concluded that the crystalline fraction is present only at the surface while the sample bulk is amorphous.

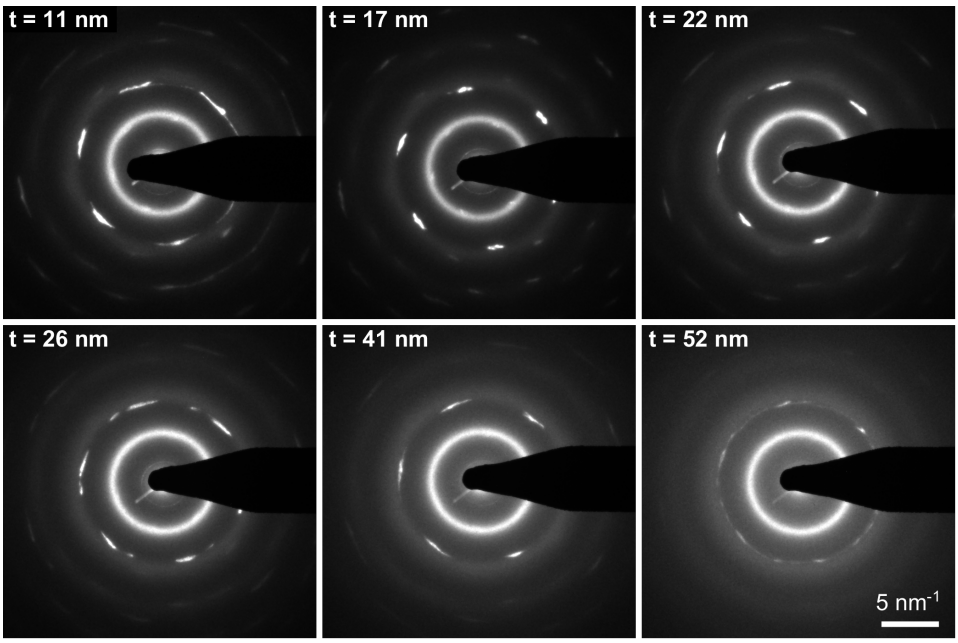

Figure 3.15: Selected area electron diffraction patterns of stress-annealed $Cu_{57}Cu_{23}P_{20}$ prepared by tripod polishing, acquired on the *Tecnai F30* (300 kV) and a camera length of 250 mm. The thickness had been determined through EELS measurements. It is indicated as t in the top-left corner of each diffraction pattern.

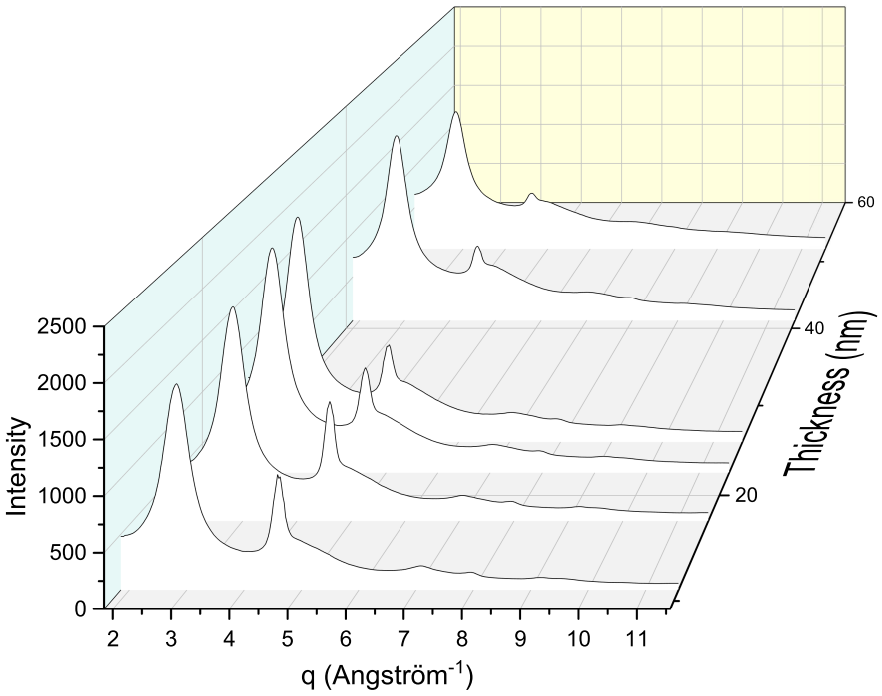

Figure 3.16: Azimuthally averaged intensity profiles of the SADPs presented in figure 3.15 plotted against the thickness of the region where the SADP have been acquired. Samples have been prepared by tripod polishing.

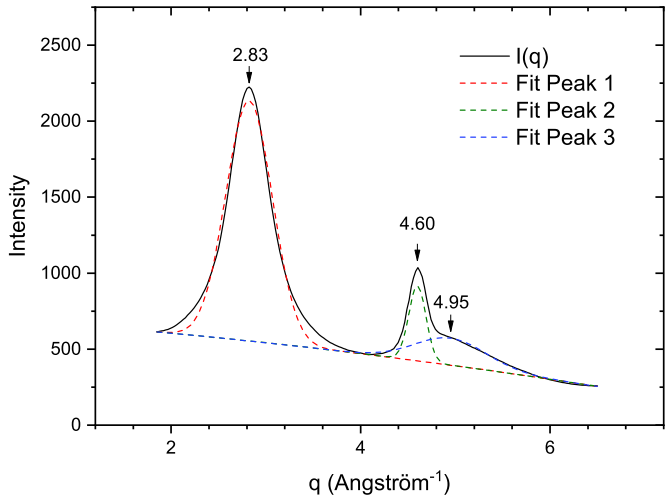

Figure 3.17: Azimuthally averaged SADP Intensity profile of PtCuP-BMG presented in figure 3.15, prepared by tripod polishing and PIPS finish, acquired at a thickness of 17 nm. The peaks have been fitted with Gaussian curves, the background with a polynomial.

3.4.3 Ultramicrotomy

The selected area diffraction pattern was despeckled in *ImageJ*, and then loaded into *eRDFAnalyser* to obtain a calibrated rotational average, showing intensity as a function of the scattering vector q. The calibrated dataset is then imported into *Origin* to perform a peak analysis. For this, the background is fitted with a parabolic function. Figure 3.19 shows the (background-corrected) azimuthally averaged intensity profile obtained from the SADP shown in figure 3.18 (b). It can seen that unlike the samples that had been exposed to an ion beam during preparation, the sectioned sample shows no indication for crystallinity.

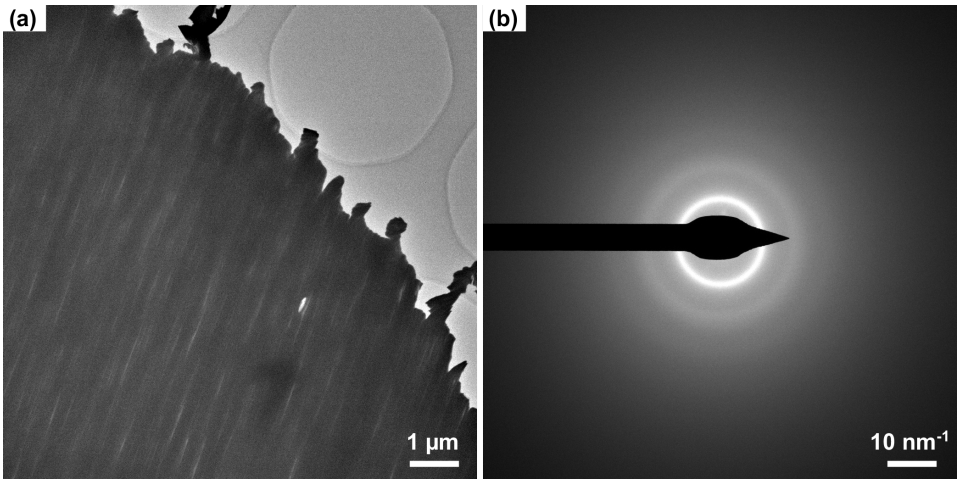

Figure 3.18: (a) Brightfield image of a ultramicrotomed section (200 kV) on a carbon grid produced using a cutting speed of 4 mm/min and a set thickness of 30 nm. Shear deformation is clearly visible, sectioning direction was normal to (b) Selected area diffraction pattern shows diffuse rings and no discrete spots that would indicate crystallinity.

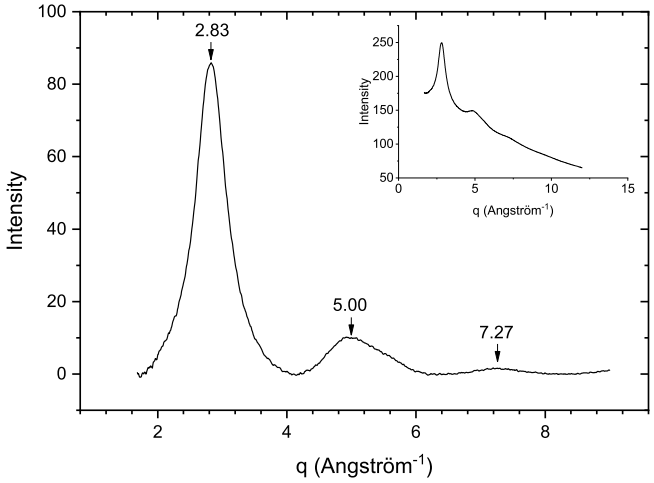

Figure 3.19: Azimuthally averaged intensity profile of the SADP presented in figure 3.18(b) of the PtCuP-BMG-specimen prepared by ultramicrotomy before (inset) and after background correction. The absence of sharp Bragg peaks as shown in 3.17 is clearly visible.

3.5 Phase analysis

To identify the system of phases present in the samples that had undergone melting and solidification TEM specimens were prepared in the FIB-SEM following the procedure described in section 2.5.4. Two samples, both non-annealed $Pt_{57}Cu_{23}P_{20}$ have been chosen for phase analysis: one had been heated to 700 °C and subsequently (and without delay) cooled to room temperature at at cooling rate of 20 $Kmin^{-1}$, the other one had been melted, crystallized and then held at 545 °C, that is 5 °C below the melting point, for 24 hours.

The data obtained from microstructure analysis using BSE-SEM and EDS-SEM(see section 2.2) provided a good overview on the elemental composition of the phases. At this point, the existence of a stoichiometric platinum-phosphor phase could already be predicted with great certainty. In preparation of electron diffraction experiments, a FIB lamella was prepared. Prior to electron diffraction analysis, a chemical map using STEM-EDS in the *FEI Talos* was acquired. This allows to roughly determine the chemical composition of the different phases in the TEM-specimen and allows to identify a limited number of candidates for each phase - a critical point when comparing acquired diffraction patterns to simulated ones of the possible candidates.

Mapping data was evaluated using the *BRUKER Esprit* software of FEI. Prior to quantifying different areas of the map, a quantification method was established consisting of four steps: (1) element identification, (2) background fit, (3) peak deconvolution and

(4) quantification. After selecting the right elements and specifying a fixed list, the background correction model 'physical (TEM)' is chosen. In peak deconvolution, the background corrected peak intensities are assigned to the selected elements according to a mathematical model. Subsequently a calculated spectrum is compared to the acquired spectrum, which allows the software to identify and analyze overlapping peaks. The 'Series Deconvolution' (series Bayes) was chosen as a deconvolution model. For step (4) the standard less quantification routines with 'PhiRhoZ' correction was chosen. Classic ZAF correction compensates for differences in deceleration of the primary electrons due to the atomic number (Z), the absorption of the primary emitted characteristic X-rays (A) and secondary fluorescence (F). [47] The PhiRhoz correction is based on the ZAF method, but presents improved results for low Z numbers through accounting for the ionization distribution (φ), depending on the mass density (ρ) and depth (z). [48]

3.5.1 PtCuP: DSC 20 K/min

As observed in figures 3.20 and 3.21, four different regions can be identified. Table 3.20 gives the results from the EDS analysis of the different regions showing one P-rich phase (A) and several ones depleted in P. Comparing the values with those gathers from SEM-EDS one can see the elevated measured Cu-content for all phases. This is due to the fact that both the *Omniprobe* grid as well as the TEM sample holder contain copper. Accuracy of EDS measurements decreases when the examined feature size is very small (due to contributions from neighboring phases). Since the D-phase-region is very small, it can be assumed that the EDS data is inaccurate.

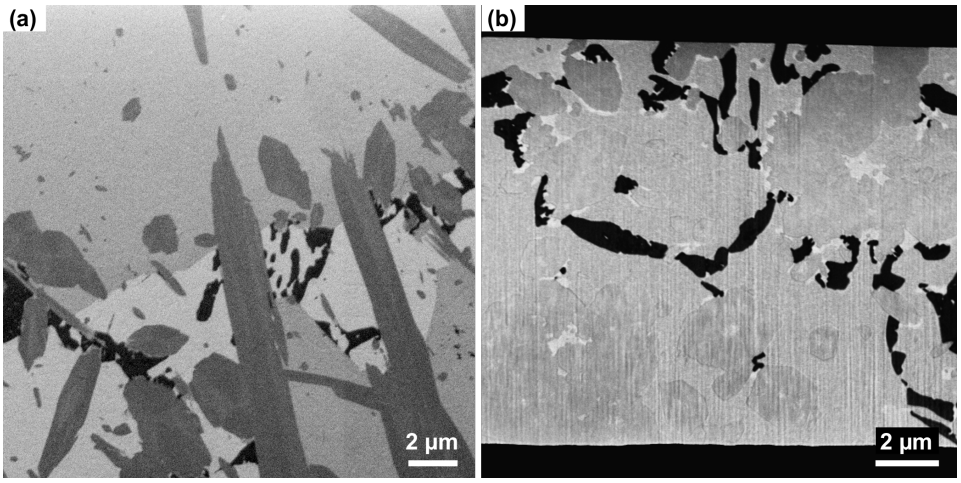

Figure 3.20: (a) Secondary electron image of the $Pt_{57}Cu_{23}P_{20}$ sample that had been heated to melt and than cooled and recrystallized at 20 K/min in the DSC, acquired in FIB-SEM. Ion polishing with Ga^+-ions yields excellent phase contrast (b) image of FIB-lamella acquired with SE-inlens detector.

A FIB lamella of the sample was prepared to perform electron diffraction with the goal to identify as many crystal structures as possible. All binary phases that have

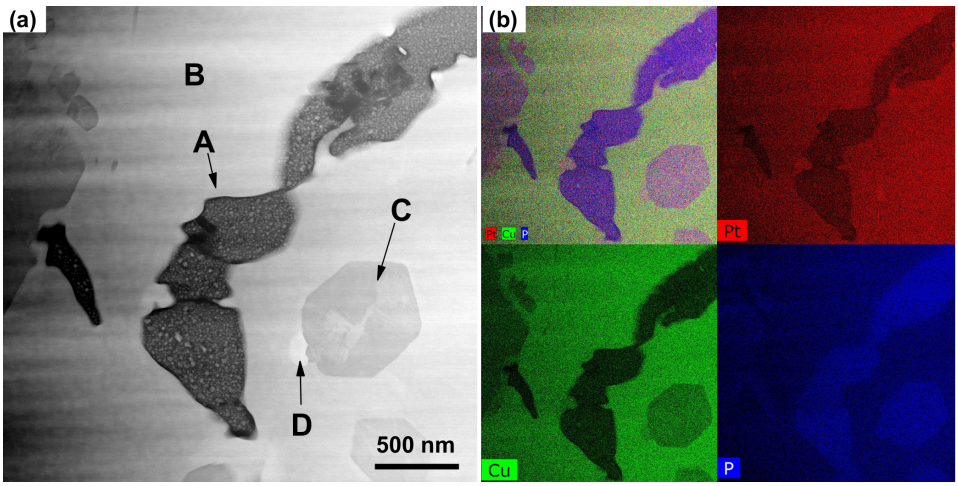

Figure 3.21: (a) STEM HAADF image revealing the different phases of the $Pt_{57}Cu_{23}P_{20}$ sample that had been heated to melt and than cooled and recrystallized at 20 K/min in the DSC. Light areas indicate phases with higher average atomic numbers. (b) Chemical map.

Table 3.7: EDS analysis results of the different regions of the $Pt_{57}Cu_{23}P_{20}$ sample that had been heated to melt and than cooled at 20 K/min in the DSC. The letters correspond to the phases specified in figure 3.21. As the method inaccuracy greatly exceeds the measured standard deviations, which are between 5 and 10 % rel., standard deviations are not provided here. Results may deviate from the actual compositions in the magnitude of 20 % and more.

	A	B	C	D
at. % Pt	28.8	46.8	45.9	49.7
at. % Cu	21.2	41.1	50.9	44.4
at. % P	50.0	12.1	3.2	5.9

previously been documented in literature are listed in 1.2. Using the both *DiffractGUI* (from the *CrysTbox* software suite) and *Single Crystal* (*Crystal Maker* software package) the patterns shown in figure 3.22 could be identified as PtP_2. PtP_2 has the cubic FeS_2 Pyrite-structure and the space group Pa-3 [49]. Figure 3.23 shows a compilation of those SADPs that could not be indexed; there are no ternary structures provided by literature. The patterns indicated with "C" could be fitted with [001] CuPt but a single zone axis is not sufficient to identify a phase with confidence. It was not possible to obtain additional zone-axis patterns.

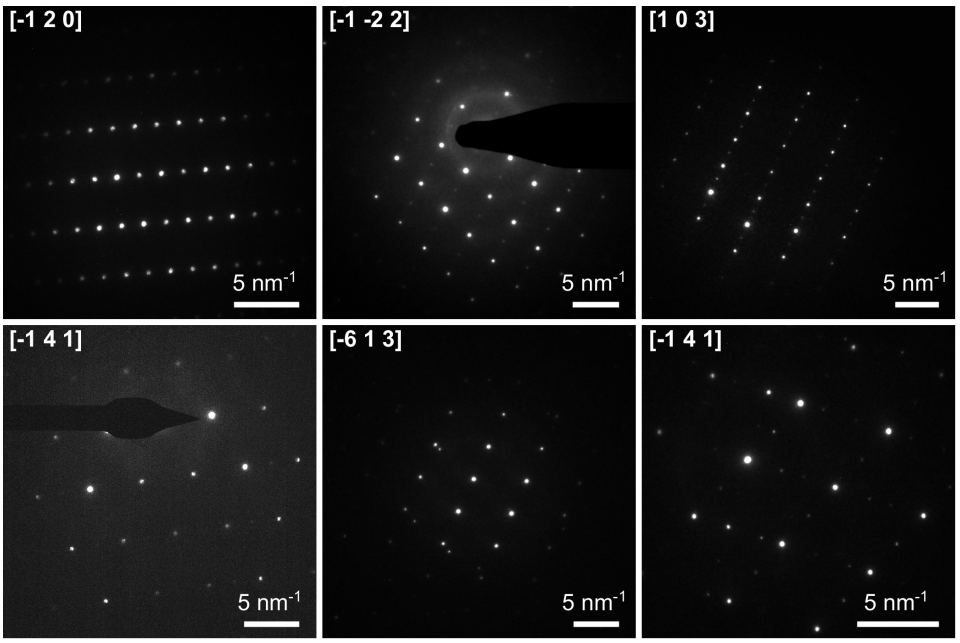

Figure 3.22: Selected area diffraction patterns of the $Pt_{57}Cu_{23}P_{20}$ sample that had been heated to melt and than cooled and recrystallized at 20 K/min in the DSC. Shown here are SADPs that were taken from phase A (see figure 3.21) which could be fitted with simulated SADPs of PtP_2. The corresponding zone axis is indicated in each pattern.

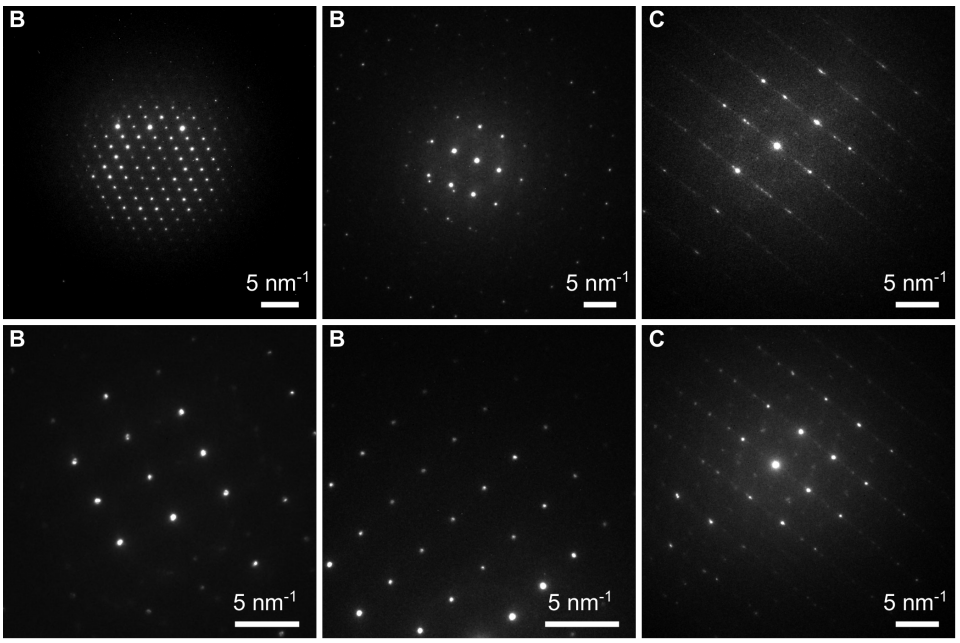

Figure 3.23: SADPs obtained from a the $Pt_{57}Cu_{23}P_{20}$ sample that had been heated to melt and than cooled and recrystallized at 20 K/min in the DSC. The four SADPs on the left correspond to phase B in figure 3.21, the two on the right to phase C. The patterns of phase C show streaks, hinting to strong deformation.

3.5.2 PtCuP: hold at 545 °C for 24 hours

Besides the DSC sample, another $Pt_{57}Cu_{23}P_{20}$ sample, which had been crystallized from the stable liquid, was characterized. This sample had been heated to melt, then crystallized and heated again to 545 °C, which is 10 °C below its melting point. To enhance grain growth and to reduce deformation of the phases, it was held there for 24 hours before it was quenched to room temperature. Figure 3.24 shows two images, both have been acquired in a FIB-SEM. It shows a bulky primary phase and a eutectic. The yellow mark in the eutectic indicates the region from where a FIB lamella was cut for TEM analysis.

Figure 3.25 shows the chemical map, which was acquired in the FIB sample. It allows to identify at least 4 different phases labeled A, B, C, D with the indicated E phase possibly coinciding with the C-phase. Table 3.8 shows the results of the EDS measurements, identifying one phase with a high P-content (A) and several low-P phases (B-E). The composition values though should only be taken as relative - the A-phase is expected to be PtP_2 without any Cu present. Since both the sample holder as well as the *Omniprobe* grid contain Cu it will always be a major element detected.

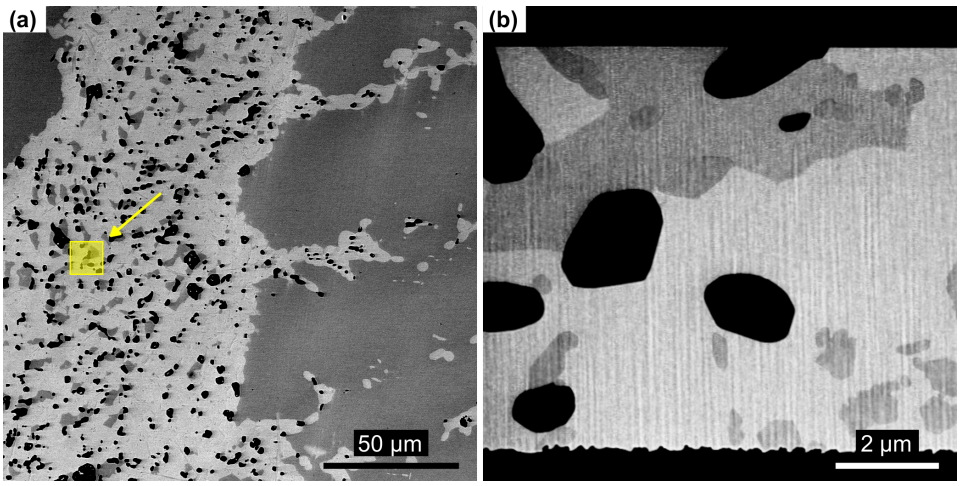

Figure 3.24: (a) SE image of 24h PtCuP sample including primary phase (wide dark grey area) and eutectic. The area from which a FIB lamella is extracted, is highlighted in yellow. (b) image of the FIB lamella. The dark phase corresponds to a phase with lower average Z than the phases that surround it.

The different phases were investigated using electron diffraction. Like in the DSC sample, the P-rich A-phase could be identified as PtP_2. Figure 3.26 shows a compilation of the SADPs. Again, selected area electron diffraction could confirm the presence of PtP_2. The other phases remain unknown as literature does not provide any more structures. There are no ternary structures characterized in literature.

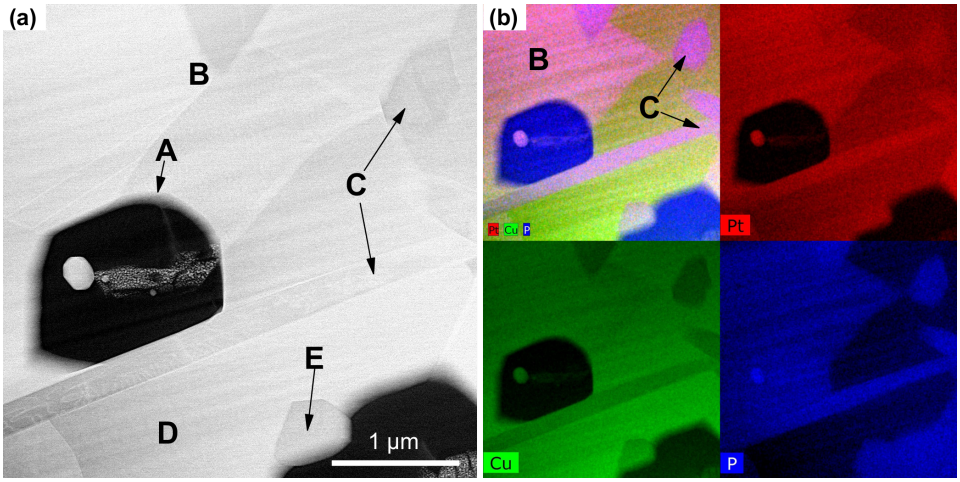

Figure 3.25: (a) STEM HAADF image of different phases in the recrystallized $Pt_{57}Cu_{23}P_{20}$ sample after 24 hours isothermal hold at 545 °C and subsequent quenching. Light areas indicate phases with higher atomic numbers. (b) Chemical map

Table 3.8: EDS analysis results of the different regions of the recrystallized $Pt_{57}Cu_{23}P_{20}$ sample after 24 hours isothermal hold at 545 °C and subsequent quenching. The letters corresponding to the different phases are specified in figure 3.25. As the method inaccuracy greatly exceeds the measured standard deviations, which are between 5 and 10 % rel., standard deviations are not provided here. Results may deviate from the actual compositions in the magnitude of 20 % and more.

	A	B	C	D	E
at. % Pt	17.6	37.8	37.5	33.4	31.8
at. % Cu	30.5	58	54.1	64.2	62.6
at. % P	51.8	4.2	8.5	2.4	5.6

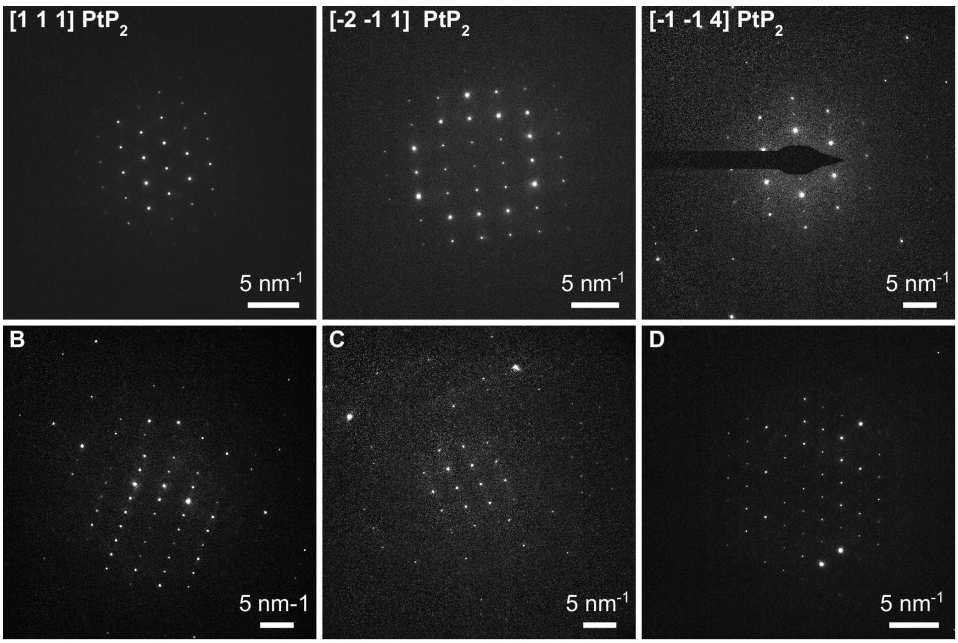

Figure 3.26: SADPs of the recrystallized $Pt_{57}Cu_{23}P_{20}$ sample after 24 hours isothermal hold at 545 °C and subsequent quenching, acquired at 200 kV on an *FEI Talos*. The top three patterns could be matched with PtP_2, the identified zone axis is indicated on the top left. The patterns at the bottom come from the phases B, C and D and could not be matched with any of the candidate structures in table 1.2.

4 Discussion

4.1 Thermophysical properties

The cooling curves in figure 3.7 show that the critical cooling rate for bypassing crystallization of $Pt_{57}Cu_{23}P_{20}$ is **4 Ks**$^{-1}$. The critical cooling rate $\dot{T}$ is roughly related to the critical casting diameter d (in cm) via equation 4.1 [50]. The critical casting thickness is therefore approximately **2.2 cm**. This is 10 % less than the values presented in figure 1.6 provided by [22].

$$\dot{T}(Ks^{-1}) \approx \frac{20}{d^2} \tag{4.1}$$

The measured values for the glass transition temperature (see table 3.4) of around 237 °C for all PtCuP BMGs are in good agreement with the values provided by the Johnson group of Caltech [22]; they measured a T_g of 235 °C. The only significant difference between the annealed and the non-annealed $Pt_{57}Cu_{23}P_{20}$ could be recognized when comparing the onset temperatures for crystallization. Whereas the T_x for the non-annealed sample lies at 303 °C, T_x is reduced to 292 °C for the annealed sample. This can be explained by formation of pre-nuclei during the annealing process.

The measured melting enthalpies (see table 3.5) range between 75 to 77 Jg^{-1}. The Johnson group has obtained values for H_m in the range of 72 to 80 Jg^{-1}.

4.2 TEM specimen preparation

4.2.1 Ion milling

At the examined conditions, ion milling alone is not a suitable method for preparing electron transparent TEM specimens from Pt-Cu-P bulk metallic glasses. Platinum is a heavy element, therefore sputter rates are low, milling times long, even under relatively "aggressive" beam conditions (energy: 5 keV, milling angle: 4 °). Comparing the diffraction patterns that were obtained from the only-ion milled (figure 3.14) and the tripod polished- and then ion milled sample (figure 3.15) one can clearly see that while in the tripod-polished specimen the spots fade out in a thickness region of around 50 nm, in the ion milled sample they persist up until very thick (diffuse) regions.

Regardless of the region, in all ion milled samples there is always a ring on 6 (or 12 due to twinning) spots that can be identified at a q-value around 4.6 nm^{-1} (just before

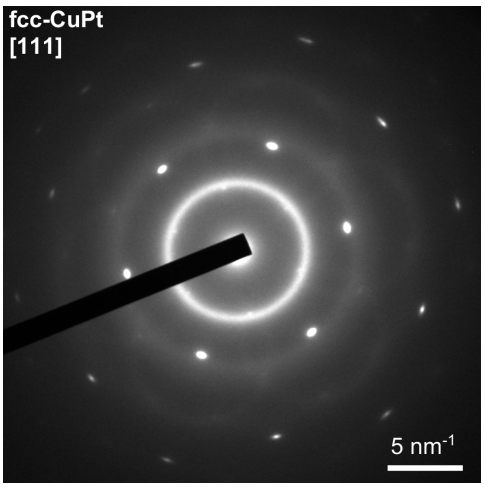

Figure 4.1: SADP of Pt-Cu-P BMG after thinning to electron transparency using ion milling (PIPS). Aside from the amorphous rings, discrete diffraction spots are clearly visible, suggesting some crystallization of the material.

the second amorphous ring at q=5nm^{-1}). The author suggests that a thin layer of CuPt (fcc, Fm-3m) preferentially grows in densely packed {111}-planes parallel to the surface. Indeed, figure 4.1 shows both amorphous rings and diffraction spots, which could be matched with the simulated SADP of fcc-CuPt using the software *Single Crystal* as part of the *Crystal Maker* software suite.

4.2.2 Tripod polishing

Tripod polishing presents a good method for pre-thinning a BMG-sample before ion milling. Following the statements of section 4.2.1 it may be possible, by finding the energy threshold for beam damage [42], to establish a combined tripod-*PIPS* preparation routine that yields samples without crystallization. Figure 4.2 shows a graph with the intensities of the deconvoluted I2 (crystalline) and I3 (second amorphous ring) plotted versus the thickness. One can clearly see that as thicker areas are reached, the crystalline peak becomes less dominant. This suggests that the crystallization is a surface property, as the volume fraction of the surface-near volume decreases linearly with increasing thickness.

4.2.3 Ultramicrotomy

Following the data presented in section 3.4.3 it can be concluded that ultramicrotomy is a very interesting method for preparing TEM specimens from bulk metallic glasses as it was the only method evaluated that did not induce any crystallization. In this respect, ultramicrotomy offers a significant advantage over other methods. General problems associated with ion beam techniques and electrolytic methods, such as beam damage, differential thinning and edge effects are completely absent or greatly reduced in this

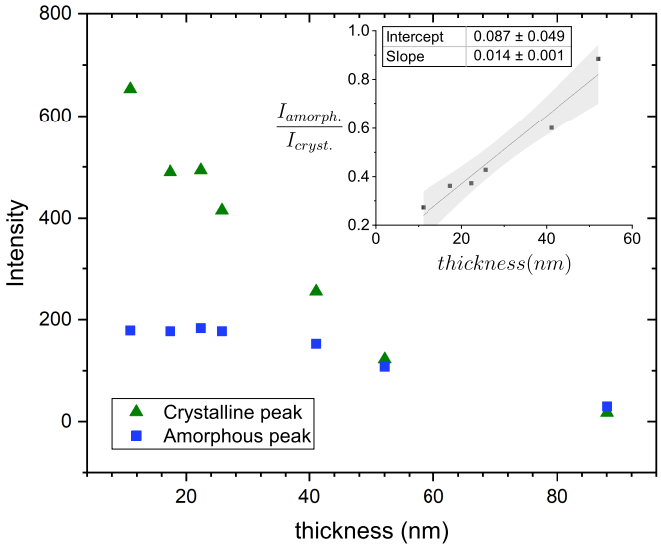

Figure 4.2: Intensiy I_2 (crystalline) and I_3 peaks (amorphous) as a function of specimen thickness after deconvolution and background correction.

process.

Cutting a metal with a knife creates a considerable amount of mechanical stress and deformation in the material, raising the question whether or not the section is structurally representative of the bulk material. The situation is entirely different in metallic glasses. BMGs have elastic limits of 1000 MPa and above, which is considerably more than most metals. This means they are a lot less prone to plastic deformation.

The quality of the specimen produced during this study is not ideal for different reasons. As ultramicrotomy is not that widely accepted in materials science (yet), which is why embedding and cutting procedures usually applied to biological samples have been followed. Since the interface between the resin and sample always broke, it is very plausible that better results would have been achieved without embedding. Furthermore, following [45], only very sharp knifes lead to good surface quality, old knifes produce streaks and ripples. It would therefore be recommended to use the best-quality knifes available.

4.3 Implementation of fluctuation electron microscopy

In the course of this study the suitability of *FEI Talos F200 X* for variable resolution fluctuation electron microscopy (VR-FEM) has been investigated. As a system with two condenser lenses, the probe size is primarily controlled by adjusting the current in the

C1-lens (spot size number). The smallest probe size that could be obtained in BF-mode was 1.6 nm using a 70 µm C2 aperture and a spot size number 8. The smallest convergence angle α was 0.5 mrad, obtained using a 10 µm C2 aperture and a spot size number 5, at the cost of a high probe size of 6 nm. Other than a low convergence angle and controllable beam size, VR-FEM requires a reasonable probe current - a criterion that could not be met a spot size numbers higher than 5 and/or a CA as small as 10 µm.

VR-FEM is a STEM technique which inherently operates with high convergence angles. Tests described above have been carried out to see what values of α can be reached under optimal conditions. The lowest α that could be achieved under regular STEM conditions was 1.5 mrad using a CA of 10 µm. However, the beam current is too low for any practical purpose. Using a CA of 70 µm under the same conditions resulted in a convergence angle on more than 10 mrad.

5 Conclusions

(1) There is little doubt that the as-received metallic glasses were completely amorphous. XRD as well as TEM data show no indication for any crystallinity. Following figure 3.2 it can be concluded that the as-received $Pt_{57}Cu_{23}P_{20}$ is fully homogeneous, featureless and without precipitates.

(2) In the course of this study different sample preparation methods (ion milling, ultramicrotomy, tripod polishing) were tried and assessed. For this purpose, a method for distinguishing surface from bulk crystallinity was developed. It depends on the evaluation of the ratio of crystalline to amorphous peak intensity as a function of sample thickness. It provides a measure on how much crystallization is induced by the preparation method.

(3) To determine the thermophysical properties of the PtCuP amorphous alloys, DSC and FDSC experiments were carried out. The DSC was calibrated using high purity metals as reference materials. The glass transition temperature T_g, the onset temperature for crystallization T_x, the onset temperature for melting T_m and the enthalpy of fusion H_m was determined. The values are in good accordance with the values provided by the Johnson group of Caltech. Using FDSC, the critical cooling rate of $Pt_{57}Cu_{23}P_{20}$ was measured.

(4) A phase analysis of the $Pt_{57}Cu_{23}P_{20}$ sample that had been recrystallized from the stable liquid was performed using SEM-EDS, STEM-EDS and selected area electron diffraction. The cubic PtP_2 could unmistakably be identified. The presence of fcc-CuPt is likely, but more zone axis patterns have to be found to identify the phase with confidence. The other phases remain unknown.

(5) The ground for implementing fluctuation electron microscopy at LMPT has been prepared. The required beam conditions could not be met on the *FEI Talos* as it only operates with two condenser lenses. It is very likely that FEM can be implemented on a different system. The accurate calibration of the *FEI Talos* with respect to convergence angle and probe size will most likely be useful for other applications.

(6) Two more alloys with the nominal compositions $Cu_{53}Cu_{27}P_{20}$ and $Cu_{53}P_{27}P_{19}B$ were prepared from PtP, CuP, Cu and Pt.

Bibliography

1. Stachurski, Z. H. *Fundamentals of Amorphous Solids: Structure and Properties* (Wiley-VCH, 2015).
2. Schroers, J. Bulk Metallic Glasses. *Physics Today* **66,** 32–37. ISSN: 0031-9228 1945-0699 (2013).
3. Cheng, Y. Q. & Ma, E. Atomic-level structure and structure-property relationship in metallic glasses. *Progress in Materials Science* **56,** 379–473. ISSN: 00796425 (2010).
4. Löffler, J. F. Recent progress in the area of bulk metallic glasses. *Zeitschrift für Metallkunde* (2006).
5. Klement, W. J., Willens, R. H. & Duwez, P. Non-crystalline Structure in Solidified Gold–Silicon Alloys. *Nature* (1960).
6. Löffler, J. F. Bulk metallic glasses. *Intermetallics* **11,** 529–540. ISSN: 09669795 (2003).
7. Inoue, A. Stabilization of metallic supercooled liquid and bulk amorphous alloys. *Acta Materialia* **48,** 279–306. ISSN: 1359-6454 (2000).
8. Technologies, L. online (https://www.liquidmetal.com/alloy/). 2018.
9. Gale, W. F. & Totemeier, T. C. *Smithells Metals Reference Book* (Elsevier, 2004).
10. *Engineering ToolBox* https://www.engineeringtoolbox.com (Accessed March 2018). 2001.
11. Inoue, A. & Takeuchi, A. Recent development and application products of bulk glassy alloys. *Acta Materialia* **59,** 2243–2267. ISSN: 13596454 (2011).
12. Kittel, C. *Introduction to Solid State Physics* 8th ed. (ed Johnson, S.) ISBN: 047141526X (John Wiley & Sons, Inc, 2005).
13. Gaskell, P. H. in. Chap. Models for the Structure of Amorphous Solids (Wiley-VCH, 2006).
14. Zhang, P., Maldonis, J. J., Besser, M. F., Kramer, M. J. & Voyles, P. M. Medium-range structure and glass forming ability in Zr–Cu–Al bulk metallic glasses. *Acta Materialia* **109,** 103–114. ISSN: 13596454 (2016).
15. Billinge, T. E. S. J. *Underneath the Bragg Peaks: Structural Analysis of Complex Materials* (2012).
16. Bernal J. D.; Mason, J. Packing of Spheres: Co-ordination of Randomly Packed Spheres. *Nature* (1960).

17. Turnbull, D. Under what conditions can a glass be formed? *Contemporary Physics* **10,** 473–488. ISSN: 0010-7514 1366-5812 (1969).

18. Cusack, N. E. *The Physics of Structurally Disordered Matter* (ed Hilger, A.) ISBN: 0852745915 (University of Sussex Press, 1987).

19. Inoue A.; Takeuchi, A. Classification of bulk metallic glasses by atomic size difference, heat of mixing and period of constituent elements and its application to characterization of the main alloying element. *Mater Trans* (2005).

20. Zhang, T. & Inoue, A. Bulk Glassy Alloys with Low Liquidus Temperature in Pt-Cu-P System. *Materials Transactions* **44,** 1143–1146. ISSN: 1345-9678 1347-5320 (2003).

21. Lu, Z. P., Li, Y. & Ng, S. C. Reduced glass transition temperature and glass forming ability of bulk glass forming alloys. *Journal of Non-Crystalline Solids* (2000).

22. Johnson, W. L. private communication. 2017.

23. Gaskell, P. New structural model for transition metal-metalloid glasses. *Nature* (1978).

24. Sheng, H. W., Luo, W. K., Alamgir, F. M., Bai, J. M. & Ma, E. Atomic packing and short-to-medium-range order in metallic glasses. *Nature* **439,** 419–25. ISSN: 1476-4687 (Electronic) 0028-0836 (Linking) (2006).

25. Egami, T. Structure of bulk amorphous P-Ni-P alloys determined by synchrotron radiation. *Metall Mater Trans* (1998).

26. Inoue, A. & Suryanarayana, C. *Bulk Metallic Glasses* ISBN: 9781420085976 (CRC Press, 2010).

27. Nishiyama, N. *et al.* The world's biggest glassy alloy ever made. *Intermetallics* **30,** 19–24. ISSN: 09669795 (2012).

28. Bachmann, K. J. & Buehler, E. Phase Equilibria and Vapor Pressures of Pure Phosphorus and of the Indium/Phosphorus System and Their Implications Regarding Crystal Growth of InP. *Journal of The Electrochemical Society* **121.** ISSN: 00134651. doi:10.1149/1.2401931 (1974).

29. Shanmugam, J., Borisenko, K. B., Chou, Y.-J. & Kirkland, A. I. eRDF Analyser: An interactive GUI for electron reduced density function analysis. *SoftwareX* **6,** 185–192. ISSN: 23527110 (2017).

30. Gmelin, E. & Sarge, S. M. Calibration of differential scanning calorimeters. *Pure and Applied Chemistry* **67.** ISSN: 1365-3075 0033-4545. doi:10.1351/pac199567111789 (1995).

31. Schneider, R. in. Chap. Energy-Dispersive X-Ray Spectroscopy (Friedbacher, G.; Bubert, H., 2011).

32. Wepf, R., Müller, E., Gramm, F., Krumeich, F. & Hafner, B. Introductory Transmission Electron Microscopy Primer (2013).

33. Williams, D. B. & Carter, B. C. *Transmission Electron Microscopy: A Textbook for Materials Science* (Springer, 2009).

34. Lugg, N. R., Kothleitner, G., Shibata, N. & Ikuhara, Y. On the quantitativeness of EDS STEM. *Ultramicroscopy* **151,** 150–9. ISSN: 1879-2723 (Electronic) 0304-3991 (Linking) (2015).

35. Hwang, J. & Voyles, P. M. Variable resolution fluctuation electron microscopy on Cu-Zr metallic glass using a wide range of coherent STEM probe size. *Microscopy and Microanalysis* **17,** 67–74. ISSN: 1435-8115 (Electronic) 1431-9276 (Linking) (2010).

36. Treacy, M. M. J., Gibson, J. M., Fan, L., Paterson, D. J. & McNulty, I. Fluctuation microscopy: a probe of medium range order. *Reports on Progress in Physics* **68,** 2899–2944. ISSN: 0034-4885 1361-6633 (2005).

37. Voyles, P. M. & Muller, D. A. Fluctuation microscopy in the STEM. *Ultramicroscopy* **93,** 147–159. ISSN: 0304-3991 (2002).

38. Yi, F., Tiemeijer, P. & Voyles, P. Flexible formation of coherent probes on an aberration corrected STEM with three condensers. *Journal of Elecron Microscopy* (2010).

39. Egerton, R. F. *Electron Energy Loss Spectroscopy in the Electron Microscope* (Springer, 2011).

40. Malis, T., Cheng, S. C. & Egerton, R. F. EELS log ratio technique for specimen-thickness measurement in the TEM. *J. Electron Microscope Technique* (1988).

41. Laub, D., Ayache, J., Beaunier, L., Boumendil, J. & Ehret, G. *Sample Preparation Handbook for Transmission Electron Microscopy* (Springer, 2010).

42. Sun, B. B. *et al.* Artifacts induced in metallic glasses during TEM sample preparation. *Scripta Materialia* **53,** 805–809. ISSN: 13596462 (2005).

43. Kelton, K. *et al.* Mechanisms for nanocrystal formation in metallic glasses. *Journal of Non-Crystalline Solids* **317.** Advances in Metallic Glasses, 71–77. ISSN: 0022-3093 (2003).

44. Bozzola, J. J. & Lonnie Dee Russell, L. D. *Electron Microscopy: Principles and Techniques for Biologists* (1999).

45. McMahon, G. & Malis, T. Ultramicrotomy of nanocrystalline materials. *Microscopy Research and Technique* **31,** 267–274. ISSN: 1097-0029 (1995).

46. Klinger, M. More features, more tools, more CrysTBox. *Journal of Applied Crystallography* **50,** 1226–1234. ISSN: 1600-5767 (2017).

47. Eriksson, M. *BRUKER: Quantification of EDS spectra* EDS User School.

48. Liao, Y. *Practical Electron Microscopy and Database (Online)* `www.globalsino.com/EM/` (2007).

49. Thomassen, L. Crystal Structures of Some Binary Compounds of Platinum Metal II (in german). *Z. Phys. Chem.* (1929).

50. Löffler, J. F., Kündig, A. A. & Dalla Torre, F. H. in *Materials Processing Handbook* chap. 17 (CRC Press, 2007).